Joule

Article

Triple-phase boundary instability as a key degradation factor in sulfide|(oxy)halide dual-electrolyte solid-state batteries

Graphical abstract

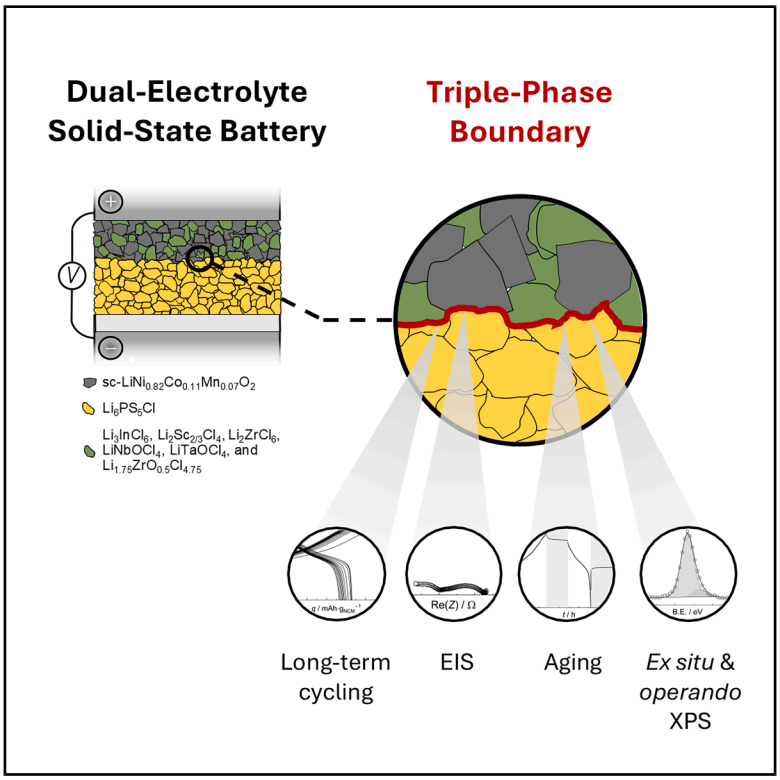

Authors

Leonardo Merola, Vipin K. Singh, Mareike Schäfer, ..., Felix H. Richter, Linda F. Nazar, Jürgen Janek

Correspondence

juergen.janek@pc.jlug.de

In brief

A sulfide|(oxy)halide dual-electrolyte solid-state battery uses a sulfide electrolyte as the separator and an (oxy)halide electrolyte in the positive electrode (cathode). The stability at the sulfide separator and (oxy)halide positive electrode interface has not yet been fully explored. This work aims to better understand the instability of this interface and study its degradation mechanism, depending on the (oxy)halide chemistry.

Highlights

- Long-term cycling of sulfide|(oxy)halide dual-electrolyte SSBs
- Analysis of the degradation products at the separator|positive electrode interface
- *Operando* XPS study of the degradation mechanism

Merola et al., 2026, Joule *10*, 102444
August 19, 2026
https://doi.org/10.1016/j.joule.2026.102444

CellPress

Joule

CellPress
OPEN ACCESS

Article

Triple-phase boundary instability as a key degradation factor in sulfide|(oxy)halide dual-electrolyte solid-state batteries

Leonardo Merola,[1] Vipin K. Singh,[2] Mareike Schäfer,[1] Elena Cortese,[1,3] Karthikeyen Natarajan Pugazhendhi,[2] Alexander Weiß,[1] Lanting Qian,[2] Shashwat Singh,[2] Sebastian L. Benz,[1] Joachim Sann,[1] Anja Bielefeld,[1] Burak Aktekin,[1] Felix H. Richter,[1] Linda F. Nazar,[2] and Jürgen Janek[1,4,5,*]

[1]Institute of Physical Chemistry, Center for Materials Research (ZfM), Justus-Liebig-Universität Gießen, Heinrich-Buff-Ring 17, 35392 Gießen, Germany

[2]Department of Chemistry and the Waterloo Institute of Nanotechnology, University of Waterloo, Waterloo, ON N2L 3G1, Canada

[3]Department of Chemical Sciences (DiSC), University of Padova, Marzolo 1, 35131 Padova, Italy

[4]Batteries and Electrochemistry Laboratory (BELLA), Institute of Nanotechnology, Karlsruhe Institute of Technology, Eggenstein-Leopoldshafen, Germany

[5]Lead contact

*Correspondence: juergen.janek@pc.jlug.de

https://doi.org/10.1016/j.joule.2026.102444

CONTEXT & SCALE To achieve the goal of commercial solid-state batteries (SSBs), the scientific community has increasingly turned to dual-electrolyte designs that combine different solid electrolytes in a single cell, each chosen for its specific advantages. A promising combination involves a sulfide as the separator electrolyte, which offers high ionic conductivity, and an (oxy)halide electrolyte in the positive electrode (cathode), which provides exceptional oxidative stability. Previous reports have shown that the novel interface between the separator electrolyte and the cathode electrolyte gets unstable, which can only be overcome by introducing an interlayer of cathode electrolyte.

This work reveals that when a sulfide and an (oxy)halide electrolyte come into contact near the cathode active material, they form a triple-phase boundary that is fundamentally unstable during cell cycling. This instability is independent of the specific (oxy)halide chemistry and leads to accelerated degradation, sulfur-gas evolution, and rapid performance decay. These findings suggest that the challenges associated with such a triple-phase boundary may be universal to other dual-electrolyte systems and could limit the practical application of dual-electrolyte SSBs. Ultimately, resolving triple-phase boundary degradation will be essential to translating dual-electrolyte SSB concepts from the laboratory-scale to real-world applications.

SUMMARY

Dual-electrolyte solid-state batteries (SSBs) that combine sulfide separators with an (oxy)halide in the positive electrode offer a promising configuration. However, most cell designs rely on additional (oxy)halide interlayers between the separator and the positive electrode. This leaves the intrinsic reactivity at the sulfide-separator|(oxy)halide positive electrode interface largely unexplored. Here, we systematically investigate this interface using Li_6PS_5Cl and six (oxy)halide solid electrolytes across three cell configurations. We show that the triple-phase boundary between the active material and two solid electrolytes is intrinsically detrimental, leading to rapid performance decay regardless of the (oxy)halide chemistry. High-capacity retention is only achieved when this boundary is avoided. *Ex situ* and *operando* X-ray photoelectron spectroscopy (XPS) reveal the formation of localized degradation products, including metal sulfides and elemental sulfur/oxidized sulfide compounds, alongside sulfur gas evolution at ~4.3 V vs. Li^+/Li. These findings identify triple-phase boundary instability as a key degradation mechanism and provide design guidelines for stable dual-electrolyte architectures.

INTRODUCTION

Lithium-ion batteries (LIBs) are essential for a wide range of applications, particularly in portable devices and electric vehicles. However, the demand for batteries with higher power and energy density, as well as improved safety, continues to grow, especially in the electric vehicle sector. In this context, solid-state batteries (SSBs) emerge as the most promising advancement over traditional LIBs. One great advantage of SSBs is that the solid electrolytes (SEs) may allow the use of lithium metal (or lithium metal alloys) as negative electrode materials. This innovation could lead to a significant increase of up to 70% in volumetric energy density and 40% in gravimetric energy density.[1,2] Nevertheless, to outperform LIBs, especially at high C-rates, SEs need an ionic conductivity of $\geq$10 mS·cm^{-1}, a wide electrochemical stability window against both positive and negative electrodes, and scalable processability.[1,2]

Sulfide-based SEs, in particular argyrodite-type SE $Li_{6-x}PS_{5-x}Cl_{1+x}$ (with $0.0 \leq x \leq 0.5$), are intensively explored in SSB research because of their high ionic conductivity,[3,4] good mechanical properties (i.e., malleability),[5–8] and stability against lithium alloys (e.g., In/InLi_x, Al/AlLi_x, and Sn/SnLi_x).[9,10] However, their low upper electrochemical stability limit (i.e., ~2.5 V vs. Li^+/Li) causes degradation reactions upon contact with the positive electrode active material, resulting in a loss of capacity during cycling.[11] In contrast, (oxy)halide SEs have a wider electrochemical stability window with a higher upper stability limit, an extensive range of compositions and structures (e.g., Li_3InCl_6 [LIC], Li_2ZrCl_6 [LZC], $Li_2Sc_{2/3}Cl_4$ [LSC], and LiMOCl$_4$ with M = Nb or Ta), and a broad range of ionic conductivity from 0.5 to 10 mS·cm^{-1}.[12–14] Despite their theoretically good electrochemical stability against positive electrode active materials (e.g., ~4.2 V vs. Li^+/Li), their stability with lithium metal (or alloys) remains a matter of debate, which restricts their use as separator materials.[13,15,16]

Apparently, neither all-sulfide-based nor all-(oxy)halide-based SSBs can achieve acceptable long-term cycling due to issues either at the positive or negative electrode, respectively. A potential solution is to use a sulfide SE as separator material in contact with lithium or a lithium alloy and an (oxy)halide SE in the positive electrode composite, forming a so-called dual-electrolyte SSB.[17,18]

The most widely reported cell configuration employs a bilayer separator cell (i.e., negative electrode|sulfide|(oxy)halide|(oxy)-halide positive electrode),[12] where an extra (oxy)halide interlayer is placed between the sulfide separator and the (oxy)halide positive electrode. Such a bilayer separator was primarily adopted to avoid electrochemical degradation at the (oxy)halide|negative electrode and sulfide|positive electrode active material interfaces, therefore focusing only on the stability of the (oxy)halide|active material interface.[19–21] While this cell architecture ensures good cycling stability, it compromises the goal of thin, low-resistance, and easy-to-process cells. Clearly, a more practical and cost-effective configuration would be a monolayer separator cell, in which the sulfide separator is in direct contact with the (oxy)halide positive electrode (i.e., negative electrode|sulfide|(oxy)halide positive electrode). Therefore, in this work, a monolayer separator cell refers to cells with a sulfide separator alone.

Interestingly, since the first studies on halide SEs from Li et al.[20,21] and Asano et al.,[22] the monolayer separator configuration was not always applied, even for newly developed (oxy)-halide SEs.[13,14,16,23–31] To date, it has only been explicitly demonstrated for the LIC-based positive electrode that a monolayer separator cell causes a lower capacity retention than a bilayer separator cell or an all-sulfide-based cell.[32] The low capacity retention of the LIC-based monolayer separator cell was demonstrated to be a consequence of the formation of indium sulfide (In–S) compounds at the sulfide separator|(oxy)halide positive electrode interface. This interface is also called a triple-phase boundary because it is shared between the sulfide, (oxy)halide, and positive electrode active material.

Whether this issue is specifically due to the reactivity of indium or is commonly shared by other halide SEs, such as Sc and Zr-based halides, or recently reported oxyhalides remains unknown, because a systematic (electro)chemical investigation of monolayer separator cells with (oxy)halides not containing indium is lacking. More importantly, any details of the electrochemical degradation mechanism at the interface between the sulfide separator and the (oxy)halide positive composite electrode (i.e., triple-phase boundary: SE_1|active material|SE_2) remain unexplored.

Inspired by this knowledge gap, we systematically compared the cycling performances of In-, Sc-, and Zr-halide (LIC, LSC, and LZC) and Nb-, Ta-, and Zr-oxyhalide SEs ($LiNbOCl_4$ [LNOC], $LiTaOCl_4$ [LTOC], and $Li_{1.75}ZrO_{0.5}Cl_{4.75}$ [LZOC]) in both monolayer- and bilayer-separator SSB cells. Results from long-term cycling, impedance spectroscopy, and electrochemical aging reveal that the triple-phase boundary formed between the positive electrode active material and the two SEs (i.e., sulfide separator|(oxy)halide positive electrode) severely compromises cell performance. In contrast, introducing an (oxy)halide interlayer to avoid this triple-phase boundary significantly improves the capacity retention. Importantly, the detrimental effect of the triple-phase boundary was consistently observed for all (oxy)halide SEs investigated. To support the electrochemical results, the formation of an SE interphase at the triple-phase boundary was confirmed through *ex situ* chemical analysis, using X-ray photoelectron spectroscopy (XPS). Additionally, *operando* XPS revealed that the degradation reaction at the triple-phase boundary occurs at $E \geq 4.3$ V vs. Li^+/Li, when the voltage exceeds the oxidation stability window of the (oxy)halide. This leads to a reaction between the (oxy)halide and sulfide SE, forming elemental sulfur/oxidized sulfide compounds (i.e., S_8 and Li_2S_n with $3 \leq n \leq 8$) and releasing sulfur gas, which is not seen in an all-sulfide-based cell. Overall, our experiments demonstrate significant electrochemical instability at the triple-phase boundary between the sulfide separator and the (oxy)halide composite positive electrode, independently of the (oxy)halide SE chemical composition and its indium content. Furthermore, our work highlights the need for future research to address the instability at the triple-phase boundary to facilitate the development of stable dual-electrolyte SSBs suitable for applications beyond laboratory scale.

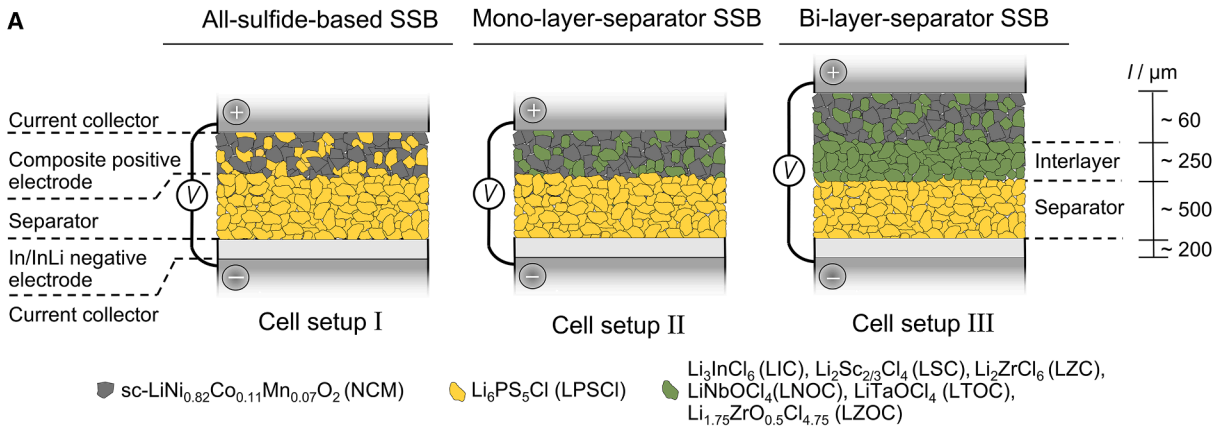

B

Cell setup	Negative electrode	Separator	Interlayer	Positive electrode
I	In/InLi	LPSCl		NCM:LPSCl
II	In/InLi	LPSCl		NCM:(Oxy)Halide
III	In/InLi	LPSCl	(Oxy)Halide	NCM:(Oxy)Halide

Figure 1. Cell setup schematics

(A) Schematic representation of the three cell setups used in this work with single-crystalline NCM as the active material (gray) for the positive electrode and In/InLi alloy as the negative electrode. The schematic of the cells is not on a real scale. For a better understanding of the cell design, the thickness (*l*) of each component is documented on the right-hand side.

(B) Composition of the cell setups used in this work.

RESULTS AND DISCUSSION

To evaluate whether the chemical incompatibility between the sulfide separator and the (oxy)halide positive electrode is limited to In-containing halide SE, we investigated an argyrodite-type SE, six different (oxy)halide SEs, and three distinct cell configurations. Li_6PS_5Cl (LPSCl) was chosen as the sulfide SE, while LIC, LSC, LZC, LNOC, LTOC, and LZOC were chosen as (oxy)-halide SEs. The cell setups are schematically depicted in Figures 1A and 1B. We define the three configurations used in this work as follows:

(1) All-sulfide-based SSB (cell setup I): a benchmark cell using only LPSCl (yellow) as electrolyte in the separator and in the positive electrode.
(2) Monolayer separator SSB (cell setup II): with LPSCl in the separator and an (oxy)halide SE (green) in the positive electrode.
(3) Bilayer separator SSB (cell setup III): LPSCl in the separator, an (oxy)halide SEs in the positive electrode, and an (oxy)halide SE as an additional interlayer between these two.

The next section provides an overview analysis of the materials and the method of composite mixing, followed by a detailed electrochemical characterization of both sulfide- and (oxy)halide-based monolayer and bilayer separator cells. This is followed by *ex situ* and *operando* XPS analyses.

We like to clarify that this study aims to systematically investigate the electrochemical behavior of monolayer and bilayer separator cells in order to determine the instability at the triple-phase boundary, and it does not focus on comparing the performance of different (oxy)halide SEs.

Characterization of materials and composite mixing

The ionic conductivities (σ_{ion}) of the SEs were determined by electrochemical impedance spectroscopy at 25°C under 80 MPa; they are calculated using Equation S1 and reported in Figure S1, showing good agreement with literature values. The X-ray patterns presented in Figure S2 confirmed the high quality of the samples and their suitability for this study, showing some minor LiCl impurities in the case of (oxy)halides SE, which is a common feature.

The particle size distributions (PSDs) of both SEs and single-crystal $LiNi_{0.82}Co_{0.11}Mn_{0.07}O_2$ (NCM), evaluated with the scanning electron microscope (SEM) images and presented in Figure S3, are comparable and in the 2- to 8-µm range, indicating negligible PSD-related effects on electrochemical performance.[33] Composite electrodes were prepared by mild planetary ball milling, maintaining a constant NCM:SE volume ratio of ~62:38 vol % (~75:25–80:20 wt %). Focused ion beam-SEM (FIB-SEM) tomography, reported in Figure S4, confirmed the uniform microstructure and target volume ratio (Tables S1 and S2).

A total of 42 working cells were cycled at 25°C, 80 MPa of stack pressure, and at a constant 0.3C rate (1*C* = 200 mAh·g^{-1}, 0.73–0.80 mA·cm^{-2}) between 2.0 and 3.7 V vs. In/InLi (i.e., 2.6–4.3 V vs. Li^+/Li) for 100 cycles. All measurements were performed in duplicates or triplicates to ensure reproducibility, and mean values and error bars were calculated using Equations S2–S4.

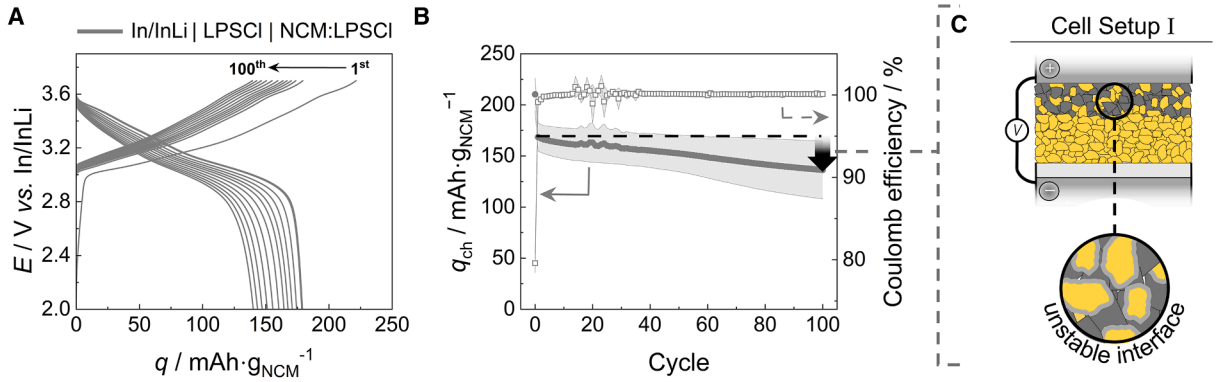

Figure 2. Long-term cycling of all-sulfide-based SSBs

(A) Charge and discharge curves of an all-sulfide-based cell setup I. The potential profiles present the 1st, 2nd, 10th, and then every 10th cycle up to the 100th cycle.
(B) Average specific charge capacity (q_{ch}) and Coulomb effciency over the cycle numbers. The error bars were calculated from triplicate measurements.
(C) Schematic representation of the cell and degradation at the sulfide|NCM interface as the main reason for capacity loss. Cells cycled at 25°C, 80 MPa, and 0.3*C* between 2.0 and 3.7 V vs. In/InLi.

All-sulfide-based SSB

The long-term cycling characterization of an all-sulfide-based SSB (i.e., cell setup I) serves as a baseline for comparison with dual-electrolyte systems incorporating (oxy)halide SEs. Figure 2A shows the evolution of the potential profile up to the 100th cycle, with a detailed description of the cell-cycling parameters reported in Figure S5. The difference between the first charge and discharge capacity mainly arises from the low voltage kinetic hindrance of NCM, which is further exacerbated in SSBs due to chemical and mechanical changes occurring during operation.[34–36]

Regarding the cycling performance, as shown in Figure 2B, the average specific charge capacity (q_{ch}) retention of cell setup I is 81% ± 10% (calculated between the 2nd and 100th cycle). Such a decrease in the capacity can be related to the formation of degradation products and contact loss at the interface between the sulfide SE and positive electrode active material, as schematically displayed in Figure 2C.[37] Overall, the evaluated electrochemical performance of the all-sulfide-based setup I is comparable with the state-of-the-art reported in literature.[4,32,33,38–40]

Sulfidel(oxy)halide monolayer and bilayer separator SSBs

Long-term cycling

Results of our detailed electrochemical investigation of the sulfide|(oxy)halide monolayer separator (cell setup II) and bilayer separator (cell setup III) SSBs are presented in Figure 3. The latter shows the average q_{ch} and Coulomb efficiency as a function of the cycle number for both cell setups II and III with (A) LIC, (B) LSC, (C) LZC, (D) LNOC, (E) LTOC, and (F) LZOC. Representative charge and discharge profiles, along with the cell-cycling parameters, are plotted in Figure S6.

The monolayer separator cells (cell setup II) with LNOC and LTOC show the highest initial q_{ch} among the presented (oxy)halide-based cells, followed by the cells with LZC, LIC, LZOC, and LSC. The bilayer separator cell (cell setup III) is characterized by a lower initial q_{ch}, compared with cell setup II. The lower initial capacity observed in cell setup III can be attributed to its higher cell resistance, which results from the presence of the additional (oxy)halide interlayer and the additional hetero-electrolyte interface between the two SEs, as discussed later in the impedance evaluation section.

Regarding the long-term cycling performance, for easier comparison, in Figure 3G, the capacity retentions of cell setups II and III are also compared with the capacity retention of the all-sulfide-based setup I. Regardless of the type of (oxy)halide SE used, all cell setups II exhibit lower capacity retention than cell setups III and, more importantly, than the all-sulfide-based cell setup I. Instead, cell setups III show a capacity retention comparable to that of the all-sulfide-based cell setup I. However, some of the cell setups III might have lower capacity retention than what is reported in literature. Such a difference can be due to the applied stack pressure during cell cycling, which differs from previous reports, but overall, this work systematically compares the cells under equivalent conditions.

The low capacity retention observed in cell setup II can be attributed to the presence of the triple-phase boundary (Figure 3H). The triple-phase boundary forms at the contact interface between the sulfide and (oxy)halide SEs close to the active material (e.g., NCM), meaning it can only form in cell setup II at the interface between the sulfide separator and the (oxy)halide composite positive electrode. Indeed, when this triple-phase boundary is avoided by introducing an additional (oxy)halide interlayer (cell setup III), the capacity retention drastically improves. We emphasize that the direct reaction at the NCM|(oxy)halide or the NCM|LPSCl interface alone does not compromise cell performance, as evidenced by the much higher capacity retention achieved in both cell setups III and I. Instead, a cooperative triple-phase boundary mechanism causes the poor performance of cell setups II.

The Coulomb efficiency further indicates a less stable cycling performance of cell setup II compared with cell setup III. Notably, cell setup II achieves values above 100%, particularly evident in

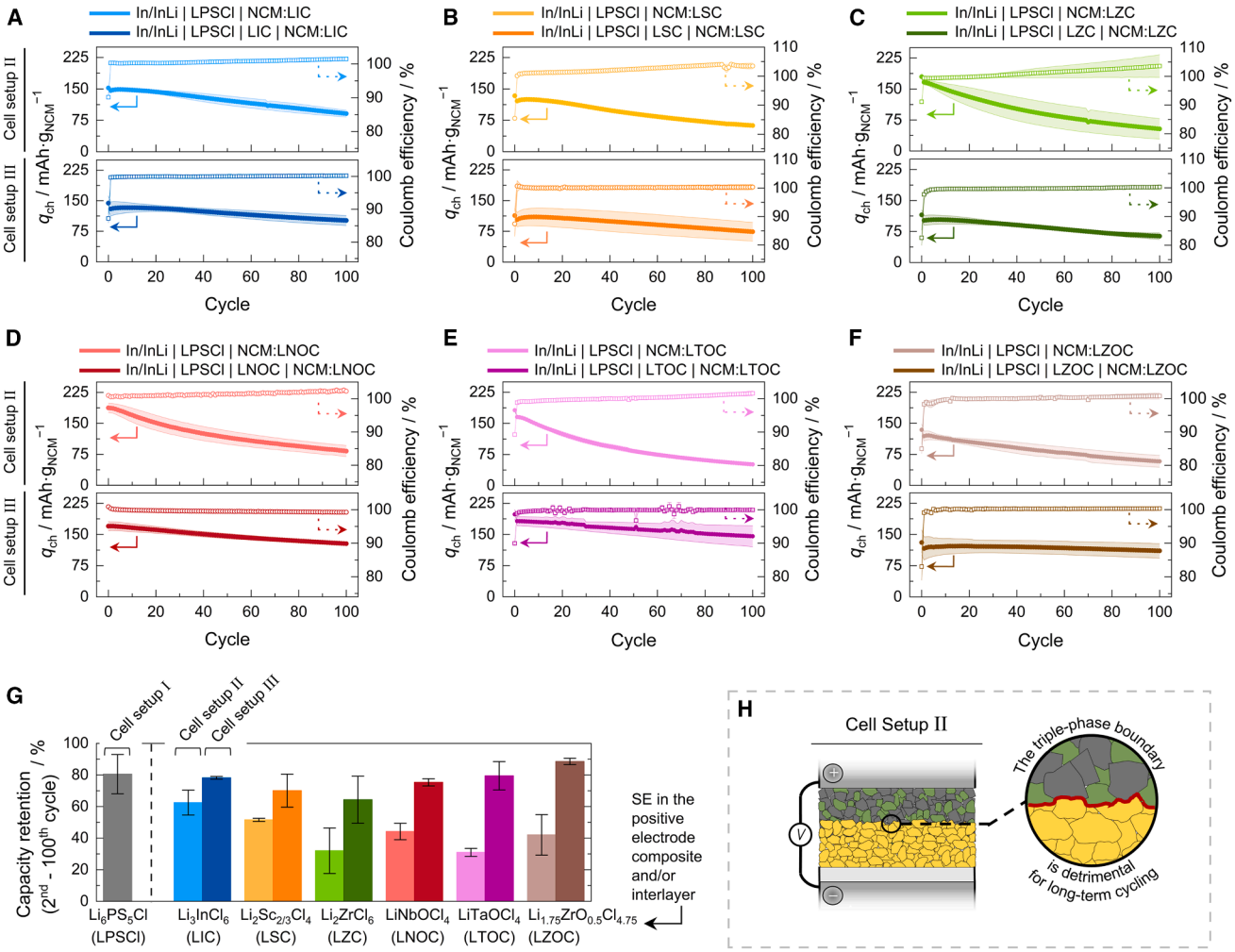

Figure 3. Long-term cycling of sulfide|(oxy)halide monolayer and bilayer separator SSBs and the detrimental effect of the triple-phase boundary

(A–F) Average charge capacity (q_{ch}) and Coulomb efficiency over the cycle number of cell setups II (up) and III (down) with (A) LIC, (B) LSC, (C) LZC, (D) LNOC, (E) LTOC, and (F) LZOC. Cells cycled at 25°C, 80 MPa, and 0.3*C* between 2.0 and 3.7 V vs. In/InLi.

(G) Comparison between the capacity retention of cell setups I, II, and III. The error bars were calculated from duplicate or triplicate measurements.

(H) Schematic representation of the triple-phase boundary interface. Such an interface is only present in cell setup II, as it is located at the sulfide separator|(oxy)halide positive electrode interface.

the case of LZC (see Figure 3C). However, despite this high efficiency of cell setups II, all cell setups III demonstrate superior capacity retention, consistently maintaining their Coulomb efficiency at nearly 100%. Although most published data for solid-state cells report values just under 100%, the persistent Coulomb efficiency >100% over many cycles for cell setup II has previously been reported by Rosenbach et al. for a LIC-based cell setup II,[32] and here, it is also confirmed for other (oxy)halide-based cell setups II. This counterintuitive trend likely reflects asymmetric resistive losses and/or side reactions limiting the charge current. Even if this explanation remains tentative owing to the limited availability of literature knowledge, these results suggest that while cell setups II exhibit higher Coulomb efficiency than cell setups III, they are more susceptible to degradation mechanisms that affect the long-term cycling performance.

Overall, based on the long-term cycling performances of the all-sulfide-based cell setup I (Figure 2) and of the (oxy)halide-based cell setups II and III (Figure 3), the detrimental effect of the triple-phase boundary in cell setup II appears to be a general phenomenon, regardless of the specific (oxy)halide SEs employed and whether they contain indium or not.

Impedance analysis

To gain further insights into the degradation processes responsible for the differences in cycle performances between cell setups II and III, impedance spectra were recorded after each charge-discharge cycle.

Figure 4A depicts the simplified equivalent circuit used to analyze the impedance data.[41–43] First, in the high-frequency region, a resistor (R_1) and a resistor in parallel with a constant-phase element (R_2/CPE_2) are used to represent the

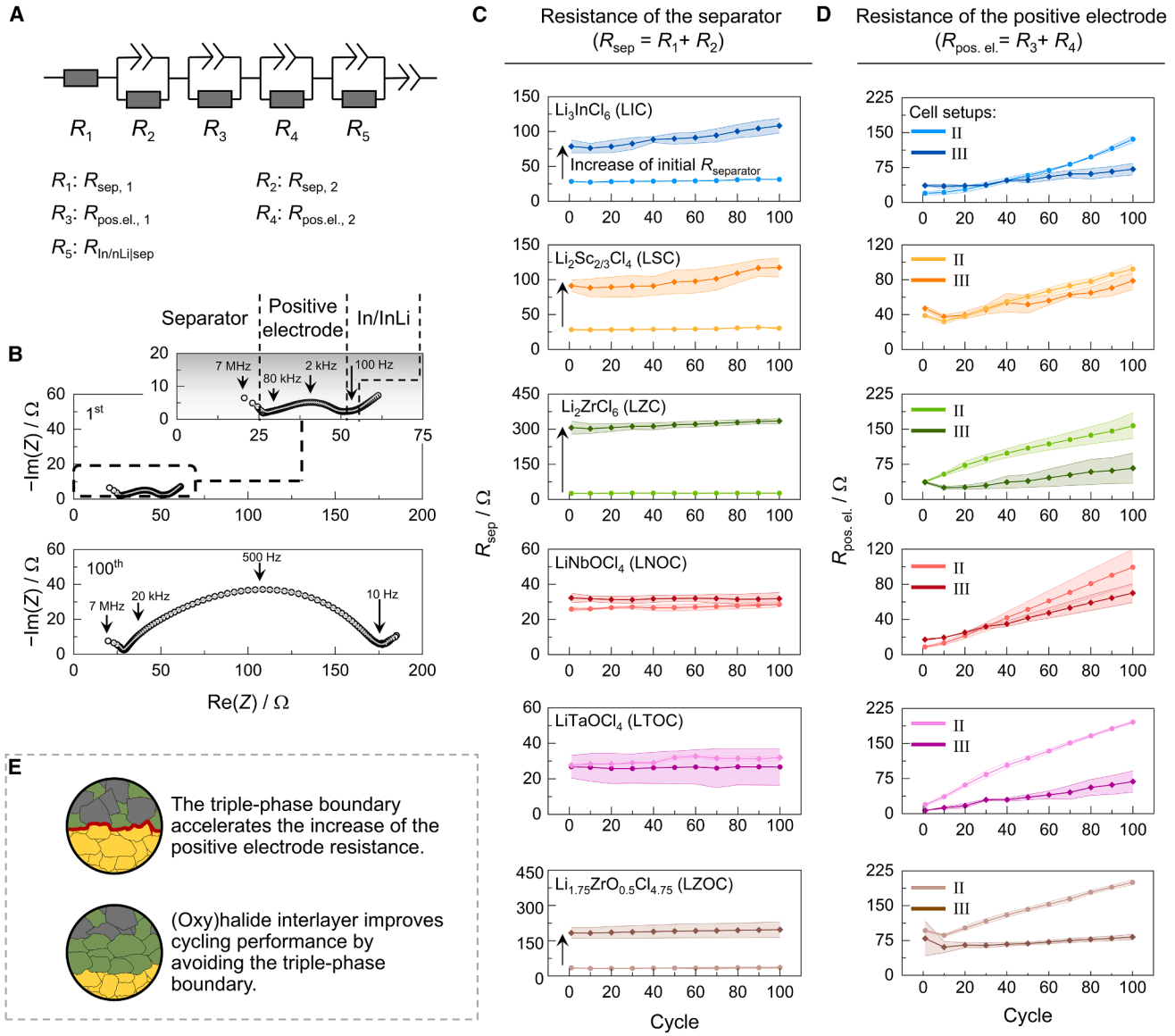

Figure 4. Comparison of the impedance evolution upon long-term cycling of sulfide|(oxy)halide monolayer and bilayer separator SSBs

(A) The equivalent circuit used to fit the impedance spectra.[32,41–43]

(B) Representative impedance spectra after the 1st and 100th charge step for cell setup II with LIC as halide SE.

(C and D) Average resistance increase of the (C) separator (R_{sep}) and (D) positive electrode ($R_{pos.el.}$) as a function of cycle number for cell setups II and III. The darker data points represent setup III. The error bars were calculated from duplicate or triplicate measurements.

(E) Summary of the conclusions from the impedance analysis.

separator. Since the contribution of the separator (R_1 and R_2/CPE) are not fully covered by the measured frequency range, it is not possible to unambiguously separate them (e.g., bulk or grain boundary). Therefore, they are presented as $R_{sep} = R_1 + R_2$.

In the mid-frequency region, two processes, represented by two resistor/CPE elements (R_3/CPE_3 and R_4/CPE_4), are associated with the composite positive electrode. These processes are distinguished based on their different capacitances (C_3 = 10^{-7}–10^{-6} F and C_4 = 10^{-6}–10^{-5} F), which were calculated with the Brug's equation.[44] However, owing to the similar time constant (i.e., apex frequency), the assignment of these processes is very challenging, and for the sake of qualitative investigation and comparisons with literature, they are presented as $R_{pos.el.} = R_3 + R_4$. We emphasize that R_3/CPE_3 and R_4/CPE_4 include all possible processes in the composite electrode, such as the interfaces, charge transfer, interphases, and geometric constriction effects within the electrode and between the composite electrode and the separator.

The low-frequency region, R_5/CPE_5, represents the interface between the negative electrode and the separator (i.e., In/InLi|sep). At low frequencies, a Warburg-type impedance describes lithium diffusion in the active material and is represented

by CPE_6. The In/InLi|sep interface (i.e., R_5) does not have a significant impact on this analysis, as it remains stable and accounts for <5%–10% of the total cell resistance (Figure S7).

Exemplary impedance spectra of cell setup II with LIC after the 1st and 100th cycle are reported in Figure 4B, from which it can be seen that the positive electrode contribution increases significantly upon cycling. The extracted resistances, capacitances, α values (CPE exponent), and associated frequency ranges of the identified processes, obtained from the equivalent circuit fitting, are provided in Table S3, along with the distribution of relaxation times (DRT) analysis in Figure S8.

For a direct comparison, the values of R_{sep} and $R_{pos.el.}$ for cell setups II and III are plotted as a function of the cycle number in Figures 4C and 4D, respectively. Regarding the R_{sep} (Figure 4C), cell setup III exhibits a higher initial resistance when compared with cell setup II (see black arrows), which is in agreement with Rosenbach et al. for the LIC-based system.[32] This higher initial resistance could be the explanation for the low initial specific charge capacity observed for cell setup III in Figure 3, and it could be associated with the conductivity of the (oxy)halide interlayer. Indeed, as the ionic conductivity increases, the initial R_{sep} values for cell setups II and III converge. For instance, LZC with the lowest ionic conductivity (Figure S1) results in a significant difference in the initial R_{sep} between the two setups. In contrast, LNOC and LTOC, with an ionic conductivity >6 $mS{\cdot}cm^{-1}$, show a minimal difference in R_{sep} between cell setups II and III.

Notably, most of the cell setups III are characterized by an increase in R_{sep} over long-term cycling. This trend can be attributed to a chemical incompatibility between the sulfide separator and the (oxy)halide interlayer, potentially leading to an interphase formation and thus increasing the resistance.[32] This increase in R_{sep} is particularly evident with In-, Sc-, and Zr-based halides, while it is not evident for the Nb-, Ta-, and Zr-based oxyhalides, suggesting a higher stability of the oxyhalide-based interlayer at the planar interface with the sulfide separator.[45,46]

Considering the $R_{pos.el.}$ (Figure 4D), cell setups II are characterized by a much larger resistance increase during cycling than cell setups III. Moreover, all the cell setups II have a much higher $R_{pos.el.}$ increase than all-sulfide-based cell setup I (Figure S9). As summarized in Figure 4E, since the primary difference between cell setups II and III is the triple-phase boundary, we conclude that the latter contributes significantly to the increase of $R_{pos.el.}$ of cell setups II during cycling, thus limiting their capacity retention regardless of the specific (oxy)halide SE in the positive electrode. Therefore, an additional (oxy)halide interlayer improves the performance of the cells by avoiding the triple-phase boundary and the resulting $R_{pos.el.}$ increase over cycling.

Electrochemical static aging

Further confirmation that the differences in cycling performance between the cell setups II and III are related to the triple-phase boundary was obtained from electrochemical static aging experiments. The results described above (Figures 2, 3, and 4) were collected using a short open circuit voltage (OCV) step between every charge-discharge cycle, as illustrated in Figure 5A. In contrast, electrochemical static aging was enforced with a prolonged 2-h OCV step after each charge and discharge step to allow for more electrochemical degradation, as depicted in Figure 5B.[19,47,48]

Figures 5C and 5D show the average q_{ch} and Coulomb efficiency over cycling for the cell setups II and III, with LIC, LZC, and LNOC as (oxy)halide SEs. Cell setups II undergo severe electrochemical degradation during static aging, while cell setups III remain, on average, stable. The dashed lines represent the data without electrochemical static aging from Figure 3. Representative charge and discharge profiles, along with the cell-cycling parameters, are plotted in Figure S10.

These findings are further supported by the impedance analysis presented in Figures 5E and 5F. The $R_{pos.el.}$ of cell setup II is characterized by a significant increase over cycling during static aging, whereas for cell setup III, no relevant differences are observed.

As shown in Figures S11 and S12, the all-sulfide-based cell setup I experiences only a slight increase in $R_{pos.el.}$, and as discussed, cell setup III does not show significant changes during static aging (Figure 5F), demonstrating that the NCM|LPSCl and NCM|(oxy)halide interface stability is not the limiting factor here. Therefore, the pronounced electrochemical aging of cell setup II can be solely attributed to the triple-phase boundary, as summarized in Figure 5G.

Chemical analysis of the triple-phase boundary

Ex situ *XPS*

The (electro)chemical degradation at the triple-phase boundary was investigated with *ex situ* XPS. As shown in Figure 6A, cycled cell setups II were retrieved, cut in half, and ion polished under vacuum (i.e., <10 Pa) and cryogenic conditions (i.e., −100°C) to prevent thermal degradation reaction between sulfide and (oxy)halide SEs.[49–51]

As reported in Figure 6B, during sample retrieval, a distinct mechanical behavior was observed; cell setup II remained structurally intact, whereas all cell setups III consistently delaminated at the sulfide separator|(oxy)halide interlayer interface, independent of the specific (oxy)halide SE. This delamination is likely related to the mechanical compatibility (i.e., interfacial adhesion) at the sulfide separator|(oxy)halide interlayer interface rather than to an (electro)chemical degradation reaction. Indeed, this delamination was also observed immediately after cell assembly, before any electrochemical measurements, and was further observed in other interface systems (e.g., garnet|sulfide),[44] suggesting a more general interfacial delamination mechanism rather than a chemistry-specific one. Nevertheless, this instability drastically hindered reliable XPS analysis of cell setup III. Consequently, because of the large number of samples and the challenging sample preparation, only LIC-, LZC-, and LNOC-based cell setups II were selected for the XPS analysis. Based on the electrochemical trends described above, analogous XPS results would be expected for the other (oxy)halide systems.

The In 3*d*, Zr 3*d*, and Nb 3*d* core-level spectra acquired at the cycled triple-phase boundary are shown in Figures 6C–6E for LIC-, LZC-, and LNOC-based cells, respectively. Spectra from the pristine SEs and the cycled NCM|(oxy)halide interface are also included for reference. The XPS measurement geometry is illustrated in Figure 6F. All samples were sputter cleaned *in situ* before acquisition to minimize adventitious surface contamination. *In situ* sputter cleaning was optimized to minimize the ion-induced damage, as documented in Figure S13. All XPS spectra

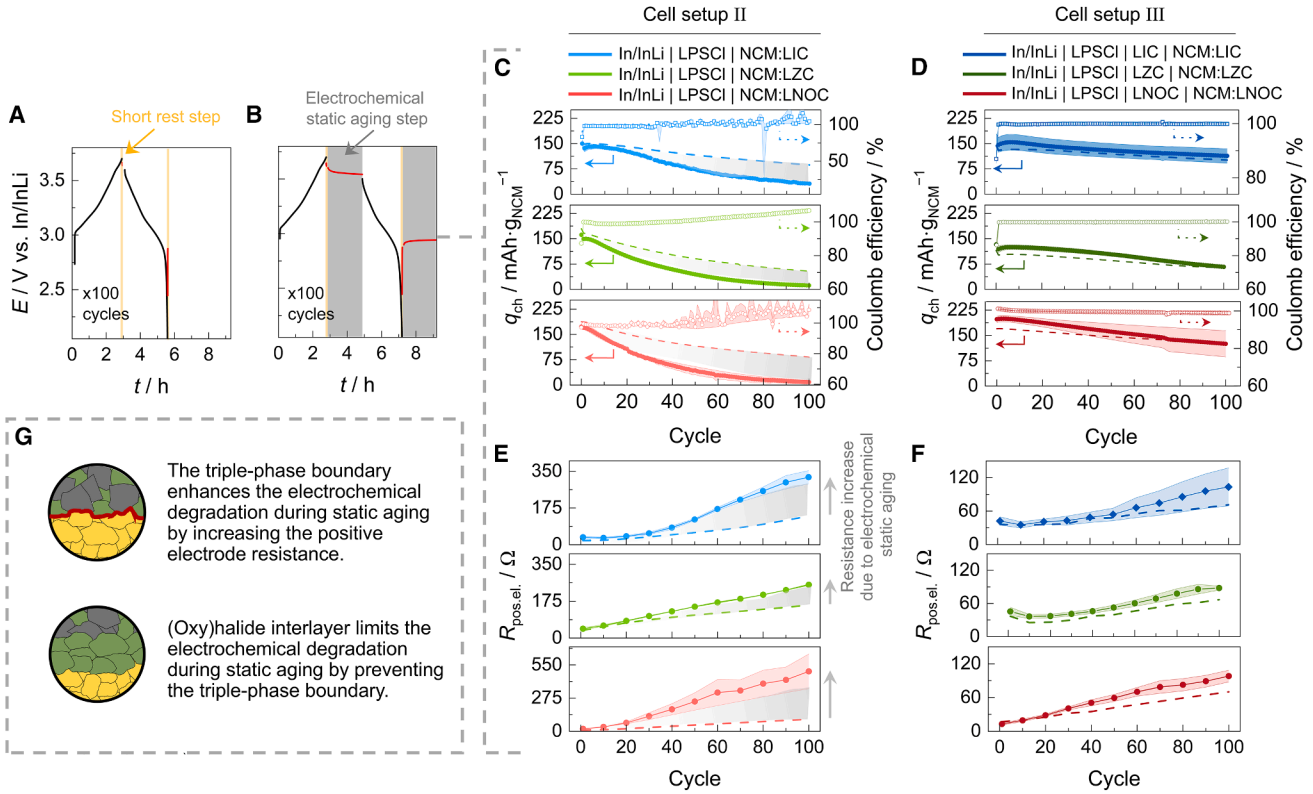

Figure 5. Effect of the electrochemical static aging on the triple-phase boundary

(A and B) Cycling conditions for (A) the results presented in Figure 3 without electrochemical aging (short rest) and (B) with electrochemical static aging.

(C and D) Average charge capacity (q_{ch}) and Coulomb efficiency over the cycle number for cell setups (C) II and (D) III during electrochemical static aging.

(E and F) Average resistance increase of the positive electrode ($R_{pos.el.}$) as a function of cycle number for cell setups (E) II and (F) III during electrochemical static aging. Cells cycled at 25°C, 80 MPa, and 0.3*C* between 2.0 and 3.7 V vs. In/InLi. The dashed lines represent the data with a short rest step from Figures 3 and 4. The error bars were calculated from duplicate or triplicate measurements.

(G) Schematic of the conclusions drawn from the electrochemical static aging study.

presented in this study were subsequently acquired under these refined conditions, ensuring consistent surface cleaning and reliable chemical analysis across all measurements. For the cycled NCM|(oxy)halide interface, which was measured directly on the retrieved positive electrode surface, the sputtering step was further employed to reduce contributions from degradation at the SE|current collector (CC) interface.[52,53]

Across all investigated (oxy)halide chemistries, *ex situ* XPS reveals consistent degradation trends, as summarized in Figure 6G. Compared with pristine materials and the cycled NCM|SE interface, the cycled triple-phase boundary shows *M*-S_x-containing compounds (e.g., *M* = In, Zr, and Nb) and elemental sulfur/oxidized sulfide compounds (e.g., S_8 and Li_2S_n where $3 \leq n \leq 8$), indicating a progressively more oxidized chemical environment. Given the chemical complexity of the systems, the In 3*d*, Zr 3*d*, and Nb 3*d* regions are discussed in detail in the main text, while the analysis of the O 1*s*, S 2*p*, P 2*p*, and Cl 2*p* regions is discussed in the supplemental information (Figures S14–S17).

For the LIC-based system, the pristine SE (Figure 6C-*i*) shows the characteristic In $3d_{5/2}$ peak at 445.8 eV.[15,20,21] At the cycled NCM|LIC interface (Figure 6C-*ii*), a new In $3d_{5/2}$ feature appears at 444.9 eV, indicating the formation of indium oxide (i.e., In–O), due to NCM|LIC interfacial degradation.[15,19,48,54–56] This assignment is consistent with the corresponding O 1*s* signal at 530.1 eV (Figure S14A).[20,35,56] At the cycled triple-phase boundary (Figure 6C-*iii*), this In–O signal intensifies, and it is renamed In–O/In–S, owing to the similar binding energies ($\Delta E_B \approx 0.1$–0.3 eV) of In–O and In–S, or generally In–S-containing compounds.[54,55] However, the reduced O 1*s* signal intensity related to In–O indicates preferential formation of In-S-containing compounds (Figure S14A). Additionally, a high-binding-energy component at 446.8 eV (Figure 6C-*iii*) appears and is attributed to indium in a highly oxidized environment or with more electronegative binding partners, such as $InCl_3$ or InOCl (i.e., In–Cl/In–OCl).[19,54] These observations are in line with computational calculations and with a similar time-of-flight secondary ion mass spectrometry (ToF-SIMS) report for LIC-based systems.[32,49]

To validate the XPS findings, ToF-SIMS analysis was conducted on the LIC-based setup II (Figures S18 and S19). The results confirm the formation of In-S-containing compounds at the triple-phase boundary, in agreement with the *ex situ* XPS analysis and consistent with the findings of Rosenbach et al.[32]

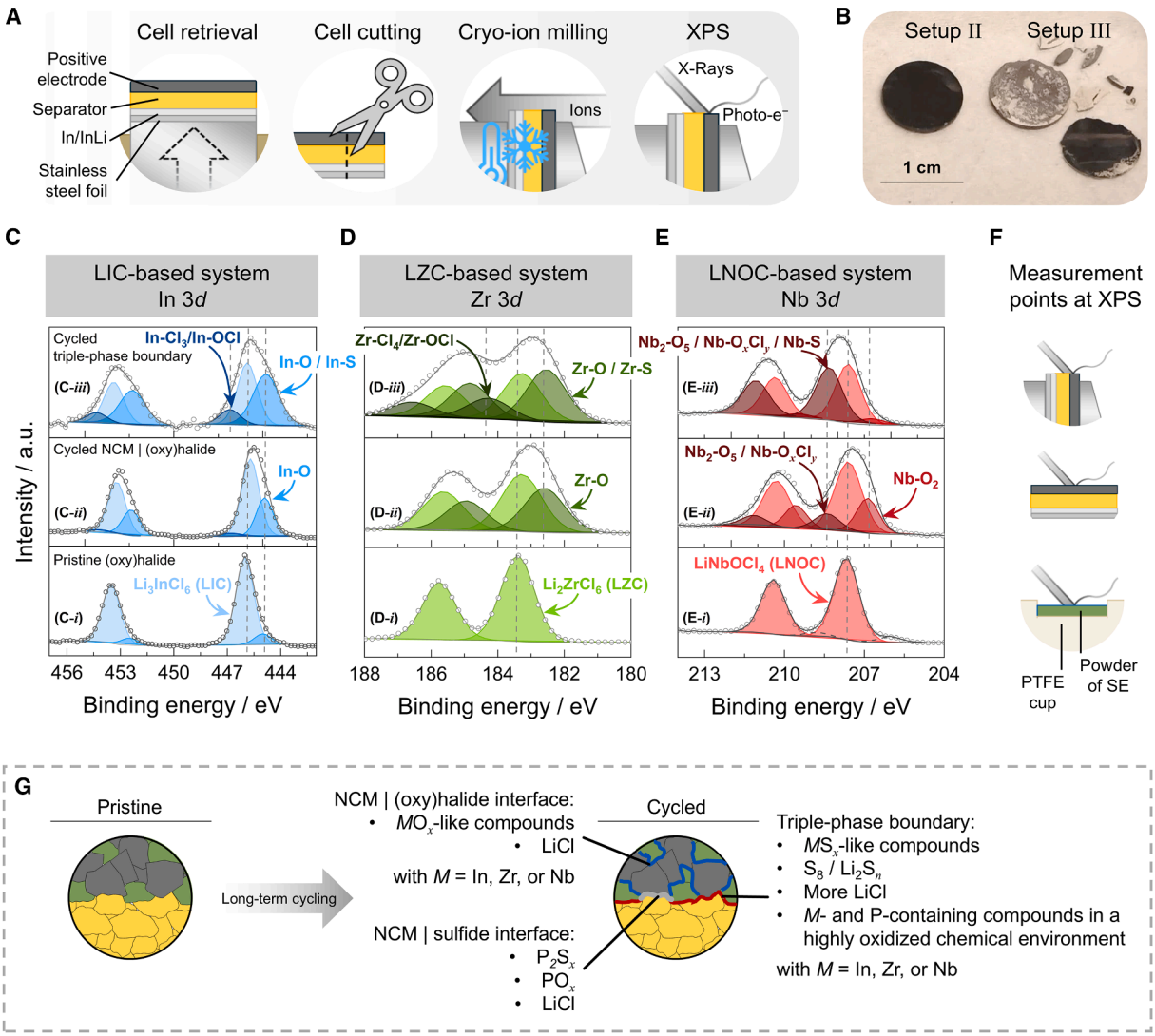

Figure 6. *Ex situ* XPS analysis to identify the electrochemical degradation products at the triple-phase boundary

(A) Schematic illustration of the sample preparation procedure for XPS analysis of the triple-phase boundary.

(B) Photograph of the cells immediately after retrieval from the cell housing.

(C–E) XPS spectra of (C) LIC-, (D) LZC-, and (E) LNOC-based samples acquired at the pristine SE (*i*), the cycled NCM|SE interface (*ii*), and the cycled triple-phase boundary (*iii*). All cycled cells with setup II were measured after 100 cycles.

(F) Schematic representation of the XPS measurement locations.

(G) Summary schematic of the identified degradation products at the NCM|sulfide, NCM|(oxy)halide, and triple-phase boundary interfaces. Here, P_2S_x = P_2S_5, $Li_2P_2S_6$, and $Li_4P_2S_7$; PO_x = Li_3PO_4 and Li_2S_n with $3 \leq n \leq 8$.

The LZC-based system shows a similar trend. The pristine SE (Figures 6D-*i*), shows the characteristic Zr $3d_{5/2}$ peak at 183.4 eV.[31,57] Upon cycling of the NCM|LZC interface, new Zr $3d_{5/2}$ and O 1*s* signals appear at 182.5 eV (Figure 6D-*ii*) and 530.5 eV (Figure S14B), respectively. These peaks indicate the formation of a zirconium oxide (i.e., Zr–O bonds).[19,58–61] At the cycled triple-phase boundary (Figure 6D-*iii*), degradation is significantly more pronounced, consistent with the very poor performance of the LZC in cell setup II. Notably, there is an increase in the intensity and shift to 182.3 eV of the Zr $3d_{5/2}$ signal, renamed Zr–O/Zr–S, to account for the fact that zirconium oxides and sulfides exhibit close binding energies ($\Delta E_B \approx 0.2$–0.5 eV).[50,62,63] The reduction of O 1*s* signal intensity associated with zirconium oxide emphasizes that Zr–S-containing compounds are the dominant degradation products at the triple-phase boundary (Figure S14B). Additionally, a high-binding-energy Zr $3d_{5/2}$ feature at 184.2 eV is detected and attributed to zirconium in a chemical environment with more electronegative binding partners, such as $ZrCl_4$ or $ZrOCl_2$. (Figure 6D-*iii*)

The LNOC-based system shows a distinct degradation pathway. The pristine SE (Figure 6E-*i*) presents the characteristic Nb $3d_{5/2}$ peak at 207.5 eV.[64] In contrast to the LIC and LZC

systems, the cycled NCM|LNOC interface (Figure 6E-*ii*) shows two additional features, contrary to what is reported for short-term cycling.[64] A Nb $3d_{5/2}$ peak at 206.8 eV can be associated with NbO_2, featuring niobium in a +4 oxidation state.[59,65] The Nb $3d_{5/2}$ second peak at 208.0 eV indicates the formation of Nb_2O_5 or NbO_xCl_y compounds (i.e., Nb_2-O_5/Nb-O_xCl_y),[55,59,65–67] with niobium in a +5 oxidation state. All these features arise from NCM|LNOC degradation; for instance, the NbO_2 signal is consistent with the reduction of LNOC around 2.15 V vs. In/InLi (Figure S6D). The formation of Nb–O-containing compounds is further supported by the appearance of a new O 1*s* peak at 530.5 eV (Figure S14C).[68,69] At the triple-phase boundary (Figure 6E-*iii*), the Nb_2–O_5/Nb–O_xCl_y feature dominates. This peak likely includes contributions from Nb–S-containing compounds (i.e., Nb–S bonds) and niobium in a highly oxidized environment; thus, it is renamed Nb_2–O_5/Nb–O_xCl_y/Nb-S.[55,67] However, this assignment remains tentative owing to the limited availability of reference spectra.

A detailed analysis of the S 2*p*, P 2*p*, and Cl 2*p* region is reported in the supplemental information (Figures S15–S17). As for the In 3*d*, Zr 3*d*, and Nb 3*d*, the analysis of the LPSCl-rated signals reveal a higher degree of degradation at the cycled triple-phase boundary than at the cycled NCM|LPSCl interface. In summary, these results show increased formation of elemental sulfur/oxidized sulfide compounds (e.g., S_8 and Li_2S_n where $3 \leq n \leq 8$), *M*–S_x-containing compounds (with *M* = In, Zr, and Nb), highly oxidized phosphorus compounds, and LiCl.

To assess the thermodynamic driving force for decomposition at the sulfide|(oxy)halide interface, first-principles calculations were carried out to identify the possible reaction pathways and their reaction enthalpies ($\Delta_r H$), as summarized in Table S4.[49,70] Although this analysis is limited to binary phase equilibria and does not include the active material (i.e., NCM), it supports the XPS findings by predicting the formation of LiCl and In–S-, Zr–S-, and Nb–S-containing compounds. Furthermore, the LPSCl|LNOC pair shows more complex reaction pathways than the LPSCl|LIC and LPSCl|LZC pairs.

Overall, the *ex situ* XPS analysis confirmed that the triple-phase boundary undergoes significantly stronger electrochemical degradation than either the NCM|sulfide or NCM|(oxy)halide interface. This localized decomposition (Figure 6G) explains the inferior cycling performance of cell setup II compared with cell setup III and particularly with respect to the all-sulfide-based setup I, regardless of the (oxy)halide SE employed or its indium content.

Operando *XPS*

To gain further insight into the degradation mechanism at the triple-phase boundary, an *operando* XPS study was conducted.[71,72] LIC was selected as the model (oxy)halide SE, and a new composite positive electrode consisting of a mixture of LPSCl, LIC, and carbon additives was prepared. This composite significantly increased the area of interest and simplified the cell design; indeed, no cross-section was needed, thereby ruling out any concerns about the impact of sample preparation. Conductive carbon additives provided an extensive interfacial area for XPS analysis, effectively mimicking the triple-phase boundary, but without the presence of active NCM material. This approach avoids contact issues from NCM volume changes and, more importantly, enables the study of interfacial reactivity between two different SEs at various potentials.

As shown in Figures 7A and 7B, the surface of this new composite was exposed to the X-ray beam, acting as the working electrode (WE). A stainless steel perforated disc was used on the top of it as the CC, ensuring sufficient stack pressure and measurable areas for the XPS analysis, as reported in Figure 7C.[71] Lithium metal was attached to the other side of the LPSCl separator and functioned as counter and reference electrodes (CE and RE).[71]

Before polarization, the *operando* cell was held at OCV overnight, and the initial state of the composite was measured at $E_{OCV} \approx 2.5$ V vs. Li^+/Li. To systematically investigate the effect of the WE potential on the triple-phase boundary oxidation, the potential was increased stepwise up to 4.7 V and then decreased back to the E_{OCV}, resulting in the staircase voltage profile in Figure 7D.[71,72] A low constant current of 50 μA was applied during polarization to minimize any cell resistance-induced overvoltage that may shift the potential at which the reactions occur. A constant voltage holding step was applied during the XPS measurements to ensure a reliable binding energy correction with respect to the applied potential.[71] The corresponding In $3d_{5/2}$ and S 2*p* spectra and component evolution are shown in Figures 7E and 7F, respectively.

At OCV, the In $3d_{5/2}$ and S 2*p* spectra show only the signals of the pristine SEs.[15,20,21,35,73] Upon polarization, LIC remains largely stable up to $E_{WE} = 4.0$ V, in line with its electrochemical stability window (~2.5–4.2 V vs. Li^+/Li),[74,75] whereas LPSCl at $E_{WE} = 3.0$ V already forms >10% polysulfides (i.e., P_2S_x = P_2S_5, $Li_2P_2S_6$, and $Li_4P_2S_7$)[72,76] and >25% at $E_{WE} = 4.0$ V, due to its much narrower stability window (~1.7–2.5 V vs. Li^+/Li).[77,78] At $E_{WE} = 4.3$ and 4.7 V, the In–Cl_3 signal rises sharply, and LPSCl degrades into both polysulfides and elemental sulfur/oxidized sulfide compounds (i.e., S_8 and Li_2S_n with $3 \leq n \leq 8$).[72,76] Even after decreasing the potential back to $E_{WE} = 4.3$ V and then to 2.5 V, these products remain, indicating irreversible decomposition at high potential.

As reported in Figure 7G, a sharp increase in chamber pressure is only observed at $E_{WE} = 4.3$ and 4.7 V, indicating gas evolution. The mass spectrometer (MS) analysis reported in Figure 7H detected mass-to-charge ratio (*m*/*z*) = 35 and 37 (chloride ions), assigned to Cl_2 gas released from LIC|carbon interface electrochemical oxidation (i.e., $Li_3InCl_6 \rightarrow LiCl + InCl_3 + Cl_2(g) + 2e^- + 2Li^+$).[79] A strong *m*/*z* = 32 signal was also detected, which could originate from either O_2 (from carbon oxidation) and/or sulfur gas (S gas, from elemental/oxidized sulfur compounds). Regarding the latter, it can likely originate from the fragmentation of a more complex molecule in the MS, as sulfur generally forms as dimers or higher oligomers in the gas phase. To distinguish between O_2 and sulfur gas contributions in the *m*/*z* = 32 signal, a pure O_2 atmosphere reference was measured to determine the characteristic counts(O_2)/counts(O) ratio during the ionization/fragmentation process in the MS (Figure S20). The pure O_2 atmosphere had counts(O_2)/counts(O) ≈ 2.75, while during the *operando* experiment, the ratio was counts(O_2)/counts(O) ≈ 7.25. This result indicates that the excess *m*/*z* = 32 intensity cannot arise from O_2 alone and is consistent with sulfur-gas

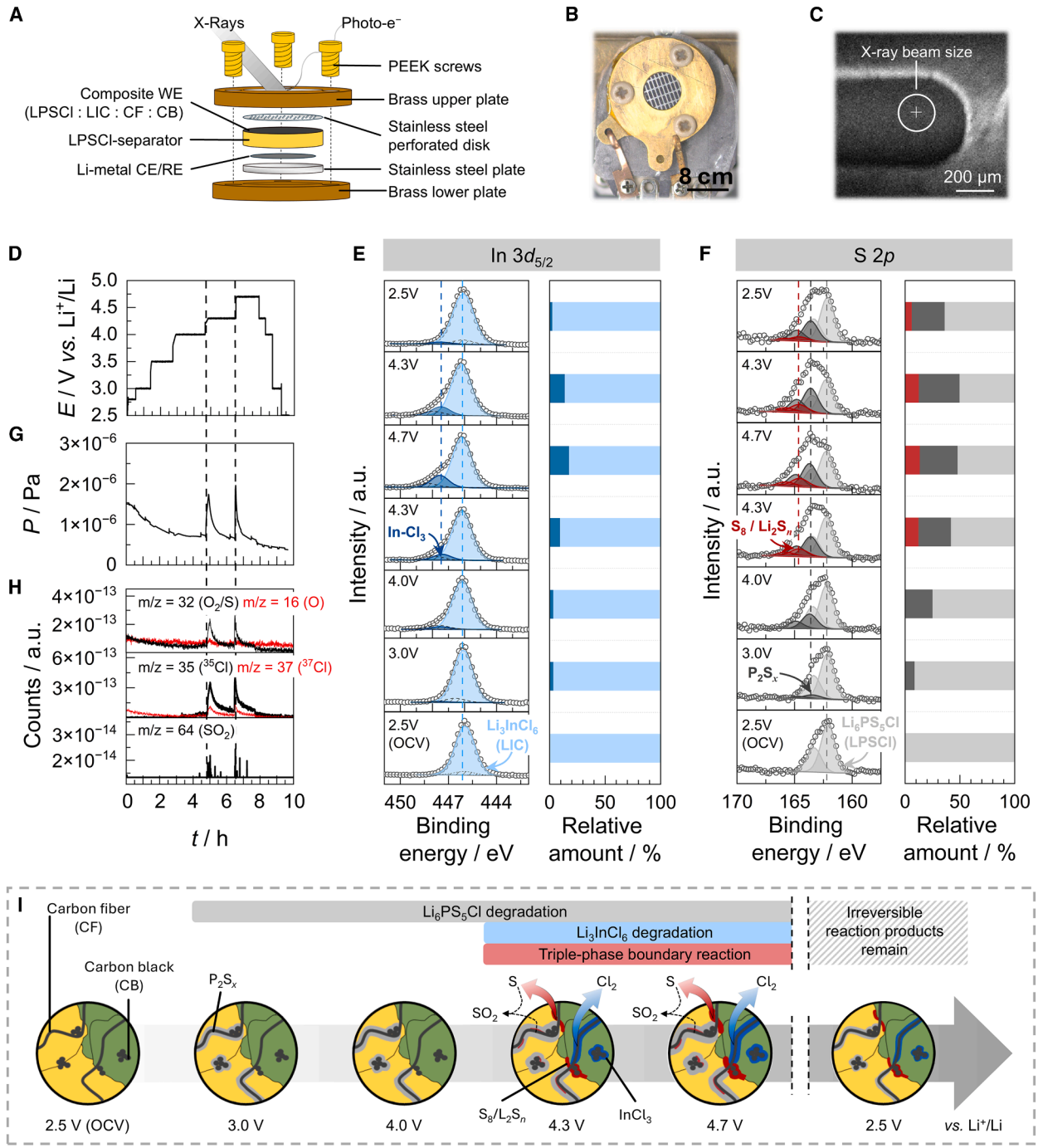

Figure 7. *Operando* XPS analysis for understanding the degradation mechanism at the triple-phase boundary

(A and B) (A) Simplified schematic representation of the *operando* XPS cell setup and (B) corresponding top-view photograph. The composite WE is composed of LPSCl (yellow), LIC (green), carbon fibers (CFs), and carbon black (CB).

(C) X-ray beam-induced secondary electron image (SXI) of the analyzed region.

(D) Constant current-constant voltage (CC-CV) polarization profile of the *operando* cell.

(E and F) XPS spectra and corresponding relative component fractions for the (E) In $3d_{5/2}$ and (F) S 2*p* regions.

(G and H) (G) Chamber pressure and (H) MS signal of the *operando* measurement.

(I) Schematic illustration of the proposed degradation mechanism at the triple-phase boundary.

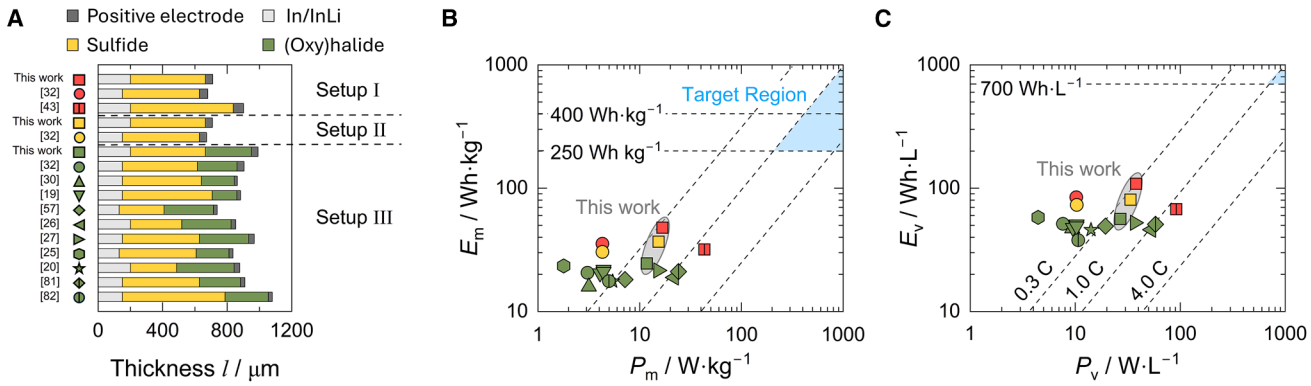

Figure 8. Comparison of the energy and power densities among the different cell setups and representative literature cases

(A–C) (A) Comparison of cell thickness (*l*), (B) gravimetric, and (C) volumetric energy (E_m, E_v) and power (P_m, P_v) densities of the cells reported in this work with representative literature cases.[19,20,25–27,30,32,43,57,81,82] Cell setups I in red symbols, cell setups II in yellow symbols, and cell setups III in green symbols. The energy and power densities were calculated as described by Randau et al.[83]

release, as sulfur gas does not generate a *m/z* = 16 fragment. A weak *m/z* = 64 signal was also observed during *operando* measurement (Figure 7H) and is attributed to SO_2, released from the LPSCl|carbon interface oxidation and from the reaction between sulfur gas with O_2 residue in the XPS chamber.[71,80]

To confirm that sulfur gas evolution and enhanced sulfur signals originate mainly from the triple-phase boundary, a control *operando* experiment, using only LPSCl and carbon (i.e., without LIC), was performed under identical conditions (Figure S21). In this case, LPSCl oxidized into polysulfides at E_{WE} = 3.0 V and elemental sulfur/oxidized sulfide compounds at E_{WE} = 4.3 V (Figures S22A and S22B) but in significantly lower amounts, and no gas release occurred at E_{WE} = 4.3 and 4.7 V (Figures S22C and S22D). This supports the results that the intensified degradation and sulfur gas release reported in Figure 7 arise specifically from processes occurring at the triple-phase boundary, in good agreement with the *ex situ* XPS results.

We summarize the proposed degradation mechanism occurring at the triple-phase boundary in Figure 7I. Upon polarization, the LPSCl begins to decompose first, forming polysulfides (e.g., P_2S_x = P_2S_5, $Li_2P_2S_6$, and $Li_4P_2S_7$), while LIC remains electrochemically stable. As the potential approaches and exceeds the stability window of LIC, the latter undergoes oxidative decomposition, generating $InCl_3$ and Cl_2 gas. This triggers a more pronounced electrochemical reaction with LPSCl and polysulfides, leading to sulfur gas evolution and the formation of large amounts of elemental sulfur/oxidized sulfide compounds (e.g., S_8 and Li_2S_n with $3 \leq n \leq 8$). When the polarization voltage is returned to the initial value, these products remain, indicating that the decomposition at high voltage is largely irreversible. During this process, the active material likely acts as a catalyst, facilitating electron transfer between the sulfide and (oxy)halide SE.

Concluding remarks and future challenges

As discussed, the triple-phase boundary between the sulfide and (oxy)halide electrolytes near the active material (e.g., NCM) is the limiting factor for dual-electrolyte sulfide|(oxy)halide SSBs. This boundary is inherently confined at the interface between the sulfide separator and the (oxy)halide positive electrode composite.

Introducing an additional (oxy)halide interlayer between the sulfide separator and the (oxy)halide positive electrode improves cycling performance, but it compromises the goal of thin SSB by increasing the cell thickness and cost. As shown in Figure 8A, the resulting dual-electrolyte configuration in cell setup III is notably thicker than the all-sulfide-based setup I, cell setup II, and literature benchmarks.[19,20,25–27,30,32,43,57,81–83] Most importantly, the resulting thicker bilayer separator lowers the energy (E_v, E_m) and power (P_v, P_m) densities, compared with that of all-sulfide-based setup I, as evidenced in the Ragone plots in Figures 8B and 8C. Consequently, despite the interfacial stabilization and good cycling performances provided by the (oxy)halide interlayer, the all-sulfide-based setup I still delivers the highest initial energy and power densities among the three configurations evaluated. Of course, in a hypothetical practical cell setup III, both the sulfide separator and any (oxy)halide interlayer would be engineered to thicknesses on the order of ~10 μm each. However, the implementation of an (oxy)halide interlayer, and an (oxy)halide-based positive electrode, would still impose gravimetric limitations, owing to the intrinsically higher density of (oxy)halide compared with sulfides, >2.2 and ~1.6 $g \cdot cm^{-3}$, respectively. Moreover, even a 10-μm additional (oxy)halide interlayer introduces extra processing steps and particularly adds material consumption, which results in higher costs of production in the end, compared with all-sulfide-based cells.

The instability at the triple-phase boundary is likely not exclusive to the sulfide|(oxy)halide systems studied here but may extend to other dual-electrolyte Li-based SSB architectures, such as Li|Al- or Ta-doped $Li_7La_3Zr_2O_{12}$|sulfide or (oxy)halide positive electrode.[44,84] Moreover, it may also extend to dual-electrolyte SSB, using different positive electrode active material (e.g., $LiFePO_4$, S_8, etc.),[85] and to Na-based SSB systems. Indeed, in a Na-SSB system with Na_3PS_4 as sulfide SE and $NaTaOCl_4$ as oxyhalide SE (Figure S23), cell setup II shows lower capacity retention, compared with cell setup III, mirroring the trends observed in Li systems.

We believe that the performance of cell setup II, specifically the instability of the triple-phase boundary in dual-electrolyte SSBs, should systematically be evaluated and reported for all dual-electrolyte SSB designs, including newly developed Li- and Na-(oxy)halide SEs. Such an assessment is as critical as understanding the stability at the active material|SE interface.

Strategies to mitigate triple-phase-boundary degradation without introducing the (oxy)halide interlayer may be required. Among these possible strategies, we can mention the following:

(1) Ultrathin coating on the sulfide separator with a material electrochemically stable against both the separator and the positive electrode composite.[86]
(2) Sulfide as the main electrolyte in the composite, but with an active material coated with a thin layer of soft (oxy)halide electrolyte, particularly using recently developed viscoplastic Al-based oxyhalides.[82,87]
(3) (Oxy)halide electrolytes that are intrinsically stable at the triple-phase boundary, for example, through fluorination, thereby eliminating the need for additional coatings or interlayers and simplifying cell architecture.[88]

Without addressing this critical instability, the relevance of sulfide|(oxy)halide dual-electrolyte SSBs would be limited to laboratory-scale demonstrations.

Conclusions

In this study, we systematically investigated the electrochemical degradation and reaction mechanisms at the triple-phase boundary in dual-electrolyte sulfide|(oxy)halide SSBs, using a sulfide separator (LPSCl) and six different (oxy)halide SEs in the positive electrode (LIC, LSC, LZC, LNOC, LTOC, LZOC). This triple-phase boundary forms only where the sulfide and (oxy)halide SE meet in proximity to the active material (e.g., NCM), specifically at the interface between the sulfide separator and the (oxy)halide positive electrode (i.e., sulfide|NCM|(oxy)halide).

Our results reveal that the detrimental effect of the triple-phase boundary on cell performances is a general phenomenon, independently of the chemistry of the specific (oxy)halide SEs employed. We confirmed the formation of localized degradation products at the triple-phase boundary with *ex situ* XPS analyses, including M–S_x-containing compounds (e.g., M = In, Zr, and Nb) and elemental sulfur/oxidized sulfide compounds (e.g., S_8 and Li_2S_n where $3 \leq n \leq 8$), which limit long-term cycling. *Operando* XPS at the triple-phase boundary further revealed the formation of these elemental sulfur/oxidized sulfide compounds and release of sulfur gas, when the cell is polarized beyond the stability limits of the (oxy)halide SE. This polarization triggers a direct reaction between the two electrolytes, during which the active material likely acts as a catalyst, facilitating electron transfer between the sulfide and (oxy)halide electrolyte.

Avoiding the triple-phase boundary by introducing an (oxy)halide interlayer between the sulfide separator and the (oxy)halide positive electrode may significantly enhance cycling stability, compared with all-sulfide-based cells. However, through our literature comparison, we show that this additional (oxy)halide interlayer increases cell thickness and weight, consequently lowering energy and power densities, compared with all-sulfide-based cells. It also requires additional processing of one more thin layer and, as a result, an increase in the production cost.

To ensure the practical applicability of dual-electrolyte SSBs is essential to address the triple-phase boundary instability through the design of innovative interfaces and engineering solutions. Among those, we can mention ultrathin separator coating, electrolyte coating on the active material, or synthesis of new and more stable (oxy)halides.

The observed instability at the triple-phase boundary likely extends beyond the materials studied here, suggesting it may also compromise other dual-electrolyte SSB systems, including sodium-based analogs. Thus, we believe that this work can establish a blueprint for future efforts to overcome the triple-phase boundary instability, a prerequisite for unlocking the full potential of dual-electrolyte SSBs.

METHODS

Materials for Li-SSBs

The LPSCl and LIC were purchased from NEI corporation. The LPSCl powder was used as received without further treatment. The LIC powder was heat-treated under vacuum in a Büchi glass oven (B-585) at 200°C for 1 h before any use. The heat treatment of LIC is necessary to remove the water from the hydrated species ($Li_3InCl_6 \cdot xH_2O$) and improve the ionic conductivity of the SE.[20] The LSC, LZC, LNOC, LTOC, and LZOC were synthesized following the reported procedure by Zhou et al.,[29] Kwak et al.,[31] Tanaka et al.,[14] and Hu et al.[13] Single-crystal (non-coated) $LiNi_{0.82}Co_{0.07}Mn_{0.11}O_2$ (NCM, $d_{10}/d_{50}/d_{90}$ = 1.7/3.3/6.1 μm) was purchased from MSE Supplies LLC and heat-treated under vacuum in a Büchi glass oven (B-585) at 250°C for 12 h before any use.

Indium foil (99.995%, 0.1 mm thickness) was purchased from chemPUR and punched into discs with a diameter of 9 mm. Lithium foil (99.999%, 0.1 mm thickness) was purchased from China Energy Lithium and punched into discs with a diameter of 6 mm. Stainless steel (SS) foil (0.020 mm thickness) was purchased from Goodfellow and punched into discs with a diameter of 9.6 mm.

All samples were handled in an argon (Ar)-filled BRAUN LABmaster glovebox ($p(O_2)/p < 0.1$ ppm, $p(H_2O)/p < 5.0$ ppm).

Positive electrode composite preparation

The positive electrode composite was prepared via planetary ball milling (Fritsch Pulverisette 7 premium line) under an Ar atmosphere ($p(O_2)/p < 0.1$ ppm, $p(H_2O)/p < 5.0$ ppm). The masses of NCM and SEs used are shown in Table S2. Materials were placed in a 45 mL ZrO_2 ball mill cup with 20 g of ZrO_2 milling balls (5 mm diameter) and mixed at 180 rpm for 15 min. The milling cups were handled in an Ar-filled BRAUN LABmaster glovebox ($p(O_2)/p < 0.1$ ppm, $p(H_2O)/p < 5.0$ ppm). The milling cups and balls were carefully dried overnight at reduced pressure in a drying cabinet (Thermo Scientific, Vacuum oven, VT 6130 M) at 60°C for 12 h.

Electrochemical characterization

All the electrochemical characterization was conducted using the VMP300 potentiostat from BioLogic Sciences Instruments

and EC-Lab software (version 11). The data were analyzed using RelaxIS 3 (version 3.0.21.17, RhD instruments, KG) software.

A detailed explanation of the homemade press cell setup used in this work can be found in our previous work.[41] Notably, the diameter of the SSB is 10 mm, resulting in an area of 0.785 cm^2. All parts of the cell were carefully dried overnight at reduced pressure in a drying cabinet (Thermo Scientific, Vacuum oven, VT 6130 M) at 60°C for 12 h.

Sulfide- and (oxy)halide-based SEs ionic conductivity

To determine the ionic conductivity of the SE, 150 mg of each powder was weighed and placed inside the homemade press cell. The material was cold densified at 3 tons (375 MPa, calculated on a 10-mm diameter) for 3 min. Stainless steel (SS) stamps were used for densification and as blocking electrodes during measurement. During the measurements, 80 MPa of stack pressure was applied. Impedance spectroscopy was conducted with the settings described below.

SSB assembly

For cell assembly, 60 mg of LPSCl was initially placed in the press cell and compacted using a hand press. For cell setups II, following this step, 12.5–14.5 mg of the composite positive electrode (with NCM loading of 12.5–13.5 $mg{\cdot}cm^{-2}$) was carefully distributed over the separator/interlayer. For cell setups III, an (oxy)halide interlayer was compacted using a hand press before adding the positive electrode composite mixture. Specific quantities of each SE were used to maintain a consistent thickness: 50.0 mg LIC, 49.4 mg LSC, 41.9 mg LZC, 51.5 mg LNOC, 58.8 mg LTOC, and 55.0 mg LZOC. Subsequently, the cell was tightened with SS stamps and cold densified at 3 tons (375 MPa, calculated on a 10-mm diameter) for 3 min, using an Atlas Autotouch 25T hydraulic press. Here, it is important to understand that the SS stamp used to compact the LPSCl separator was changed to a new one to press the (oxy)halide interlayer and composite electrode. This was done to avoid contamination of sulfide SE on the top of the interlayer and composite electrode.

After densification, the cell was opened from the negative electrode side to prepare the In-Li alloy. To ensure a suitable composition for stable cycling, a piece of indium foil (0.1 mm thickness, 9 mm diameter) was first placed in contact with the LPSCl separator, followed by a lithium foil (0.1 mm thickness, 6 mm diameter). Additionally, to facilitate the removal of the cell for postmortem analysis, an SS foil (0.02 mm thickness, 9.6 mm diameter, Goodfellow, AISI 304) was positioned on top of the In-Li alloy. The cell was then closed again and fixed in an SS frame with 80 MPa of stack pressure applied.

SSB cycling

After 5 h of microstructural equilibration, all the Li cells were cycled at a constant *C*-rate of 0.3*C* (1*C* = 200 $mAh{\cdot}g^{-1}$) between 2.0 and 3.7 V vs. In/InLi, which corresponds to 2.6 and 4.3 V vs. Li^+/Li. After every charge and discharge step, a 5-min OCV was recorded, followed by an impedance measurement. The latter was carried out with the setting described below.

For the aging experiment, the same cycling conditions were used, with the exception that 2 h of OCV was added after the impedance measurement.

EIS

Electrochemical impedance spectroscopy (PEIS or EIS) was carried out between 7 MHz and 100 mHz with a voltage amplitude of 10 mV. Points per decade and waiting time were set to 15 and 0.4, respectively. The total time required for an impedance was around ~6 min.

DRT analyses were conducted using Gaussian base functions and a regulation parameter λ of 0.01.

Na-based dual-electrolyte SSB

All the details regarding the synthesis of the materials, positive electrode preparation, battery assembling, and cycling can be found in the supplemental methods.

Characterization techniques

The X-ray diffraction (XRD) patterns, SEM, FIB-SEM tomography, *ex-situ* XPS, *ex situ* ToF-SIMS, and *operando* XPS were all conducted with in-house instruments. Most importantly, the samples were transferred to instruments using air-free transfer modules.

All the details regarding the instruments, sample preparation, sample transfer, and measuring settings can be found in the supplemental methods.

Energy and power density calculations

All the details regarding the energy and power density calculations, as well as necessary approximations, can be found in the supplemental methods.

RESOURCE AVAILABILITY

Lead contact

Requests for further information and resources should be directed to and will be fulfilled by the lead contact, Jürgen Janek (juergen.janek@pc.jlug.de).

Materials availability

This study did not generate new, unique reagents.

Data and code availability

All data reported in this paper will be shared by the lead contact upon request.

ACKNOWLEDGMENTS

The authors would like to acknowledge René Rekers for assisting in the PSD analysis, Travis Casagrande and Joseph Deering (CCEM) for the FIB-SEM tomography and reconstruction, Johannes Westphal for *operando* XPS cell assembly, and Chanhyun Park for the fruitful discussions on the degradation mechanism. E.C. acknowledges the double degree program in chemistry between the University of Padova and the Justus Liebig University. This work was conducted as part of the US-German project collaboration on "Interfaces and Interphases in Rechargeable Li-metal based Batteries" supported by the US Department of Energy (DOE) and the German Federal Ministry of Research, Technology, and Space (BMFTR). L.M. and J.J. acknowledge financial support from the German Federal Ministry of Research, Technology, and Space (BMFTR) under the project "CatSE 2" (grant identifier 03XP0510E). B.A. and J.J. acknowledge financial support from the German Federal Ministry of Research, Technology, and Space (BMFTR) under the projects "FB2-Char" and "FB2-Thio" (grant identifiers 03XP0433D and 02XP0430A). A.W. and A.B. acknowledge financial support from the German Federal Ministry of Research, Technology, and Space (BMFTR) under the project "SiMba" (grant identifier 03XP0584). V.K.S., K.N.P., L.Q., S.S., and L.F.N. acknowledge financial support from the Ontario Research Fund (ORF-RE, grant number RE-010-068) and NSERC for platform support through the Discovery and Canada Research Chair Programs.

AUTHOR CONTRIBUTIONS

L.M., conceptualization, design of experiments, formal electrochemical analysis, *ex situ* and *operando* XPS investigation, visualization, review and editing, and writing original draft; V.K.S., synthesis of oxyhalide-based SEs, design of experiments, visualization, and review; M.S., E.C., and K.N.P., electrochemical investigation and review; A.W., ToF-SIMS investigation and review; L.Q., synthesis of halide-based SEs and review; S.S., electrochemical investigation of Na cells and review; S.L.B. and J.S., investigation and validation of the *operando* XPS and review; A.B., funding acquisition, supervision, and review; B.A., conceptualization, supervision, investigation of the *operando* XPS, and review; F.H.R., supervision, visualization, validation, review, and editing; and L.F.N. and J.J., conceptualization, funding acquisition, supervision, visualization, validation, review, and editing.

DECLARATION OF INTERESTS

The authors declare no competing interests.

DECLARATION OF GENERATIVE AI AND AI-ASSISTED TECHNOLOGIES IN THE WRITING PROCESS

During the preparation of this work, the authors used ChatGPT and DeepL to improve readability and language. After using this tool, the authors reviewed and edited the content as needed and take full responsibility for the content of the published article.

SUPPLEMENTAL INFORMATION

Supplemental information can be found online at https://doi.org/10.1016/j.joule.2026.102444.

Received: December 16, 2025
Revised: February 25, 2026
Accepted: April 2, 2026
Published: May 4, 2026

REFERENCES

1. Janek, J., and Zeier, W.G. (2016). A solid future for battery development. Nat Energy *1*, 16141. https://doi.org/10.1038/nenergy.2016.141.
2. Janek, J., and Zeier, W.G. (2023). Challenges in speeding up solid-state battery development. Nat. Energy *8*, 230–240. https://doi.org/10.1038/s41560-023-01208-9.
3. Adeli, P., Bazak, J.D., Park, K.H., Kochetkov, I., Huq, A., Goward, G.R., and Nazar, L.F. (2019). Boosting Solid-State Diffusivity and Conductivity in Lithium Superionic Argyrodites by Halide Substitution. Angew. Chem. Int. Ed. Engl. *58*, 8681–8686. https://doi.org/10.1002/anie.201814222.
4. Zuo, T.-T., Walther, F., Teo, J.H., Rueß, R., Wang, Y., Rohnke, M., Schröder, D., Nazar, L.F., and Janek, J. (2023). Impact of the Chlorination of Lithium Argyrodites on the Electrolyte/Cathode Interface in Solid-State Batteries. Angew. Chem. Int. Ed. Engl. *62*, e202213228. https://doi.org/10.1002/anie.202213228.
5. Papakyriakou, M., Lu, M., Liu, Y., Liu, Z., Chen, H., McDowell, M.T., and Xia, S. (2021). Mechanical behavior of inorganic lithium-conducting solid electrolytes. J. Power Sources *516*, 230672. https://doi.org/10.1016/j.jpowsour.2021.230672.
6. McGrogan, F.P., Swamy, T., Bishop, S.R., Eggleton, E., Porz, L., Chen, X., Chiang, Y.-M., and van Vliet, K.J. (2017). Compliant Yet Brittle Mechanical Behavior of Li 2 S–P 2 S 5 Lithium-Ion-Conducting Solid Electrolyte. Adv. Energy Mater. *7*, 1602011.
7. Ke, X., Wang, Y., Ren, G., and Yuan, C. (2020). Towards rational mechanical design of inorganic solid electrolytes for all-solid-state lithium ion batteries. Energy Storage Mater. *26*, 313–324. https://doi.org/10.1016/j.ensm.2019.08.029.
8. Hikima, K., Totani, M., Obokata, S., Muto, H., and Matsuda, A. (2022). Mechanical Properties of Sulfide-Type Solid Electrolytes Analyzed by Indentation Methods. ACS Appl. Energy Mater. *5*, 2349–2355. https://doi.org/10.1021/acsaem.1c03829.
9. Santhosha, A.L., Medenbach, L., Buchheim, J.R., and Adelhelm, P. (2019). The Indium–Lithium Electrode in Solid-State Lithium-Ion Batteries: Phase Formation, Redox Potentials, and Interface Stability. Batteries Supercaps *2*, 524–529. https://doi.org/10.1002/batt.201800149.
10. Jeong, W.J., Wang, C., Yoon, S.G., Liu, Y., Chen, T., and McDowell, M.T. (2024). Electrochemical behavior of elemental alloy anodes in solid-state batteries. ACS Energy Lett. *9*, 2554–2563. https://doi.org/10.1021/acsenergylett.4c00915.
11. Auvergniot, J., Cassel, A., Ledeuil, J.-B., Viallet, V., Seznec, V., and Dedryvère, R. (2017). Interface Stability of Argyrodite Li 6 PS 5 Cl toward LiCoO 2 , LiNi 1/3 Co 1/3 Mn 1/3 O 2 , and LiMn 2 O 4 in Bulk All-Solid-State Batteries. Chem. Mater. *29*, 3883–3890. https://doi.org/10.1021/acs.chemmater.6b04990.
12. Tao, B., Zhong, D., Li, H., Wang, G., and Chang, H. (2023). Halide solid-state electrolytes for all-solid-state batteries: structural design, synthesis, environmental stability, interface optimization and challenges. Chem. Sci. *14*, 8693–8722. https://doi.org/10.1039/D3SC02093B.
13. Hu, L., Wang, J., Wang, K., Gu, Z., Xi, Z., Li, H., Chen, F., Wang, Y., Li, Z., and Ma, C. (2023). A cost-effective, ionically conductive and compressible oxychloride solid-state electrolyte for stable all-solid-state lithium-based batteries. Nat. Commun. *14*, 3807. https://doi.org/10.1038/s41467-023-39522-1.
14. Tanaka, Y., Ueno, K., Mizuno, K., Takeuchi, K., Asano, T., and Sakai, A. (2023). New Oxyhalide Solid Electrolytes with High Lithium Ionic Conductivity 10 mS cm-1 for All-Solid-State Batteries. Angewandte Chemie. Angew. Chem. Int. Ed. Engl. *62*, e202217581. https://doi.org/10.1002/anie.202217581.
15. Riegger, L.M., Schlem, R., Sann, J., Zeier, W.G., and Janek, J. (2021). Lithium-Metal Anode Instability of the Superionic Halide Solid Electrolytes and the Implications for Solid-State Batteries. Angew. Chem. Int. Ed. Engl. *60*, 6718–6723. https://doi.org/10.1002/anie.202015238.
16. Wang, C., Liang, J., Luo, J., Liu, J., Li, X., Zhao, F., Li, R., Huang, H., Zhao, S., Zhang, L., et al. (2021). A universal wet-chemistry synthesis of solid-state halide electrolytes for all-solid-state lithium-metal batteries. Sci. Adv. *7*, eabh1896. https://doi.org/10.1126/sciadv.abh1896.
17. Sen, S., and Richter, F.H. (2023). Typology of Battery Cells - From Liquid to Solid Electrolytes. Adv. Sci. *10*, e2303985. https://doi.org/10.1002/advs.202303985.
18. Schmaltz, T., Hartmann, F., Wicke, T., Weymann, L., Neef, C., and Janek, J. (2023). A Roadmap for Solid-State Batteries. Adv. Energy Mater. *13*, 2301886. https://doi.org/10.1002/aenm.202301886.
19. Kochetkov, I., Zuo, T.-T., Ruess, R., Singh, B., Zhou, L., Kaup, K., Janek, J., and Nazar, L. (2022). Different interfacial reactivity of lithium metal chloride electrolytes with high voltage cathodes determines solid-state battery performance. Energy Environ. Sci. *15*, 3933–3944. https://doi.org/10.1039/D2EE00803C.
20. Li, X., Liang, J., Chen, N., Luo, J., Adair, K.R., Wang, C., Banis, M.N., Sham, T.-K., Zhang, L., Zhao, S., et al. (2019). Water-Mediated Synthesis of a Superionic Halide Solid Electrolyte. Angew. Chem. *131*, 16579–16584.
21. Li, X., Liang, J., Luo, J., Norouzi Banis, M., Wang, C., Li, W., Deng, S., Yu, C., Zhao, F., Hu, Y., et al. (2019). Air-stable Li 3 InCl 6 electrolyte with high voltage compatibility for all-solid-state batteries. Energy Environ. Sci. *12*, 2665–2671.
22. Asano, T., Sakai, A., Ouchi, S., Sakaida, M., Miyazaki, A., and Hasegawa, S. (2018). Solid Halide Electrolytes with High Lithium-Ion Conductivity for Application in 4 V Class Bulk-Type All-Solid-State Batteries. Adv. Mater. *30*, e1803075. https://doi.org/10.1002/adma.201803075.
23. Kim, S., Lee, Y., Kim, K., Wood, B.C., Han, S.S., and Yu, S. (2024). Fluorine-Substituted Lithium Chloride Solid Electrolytes for High-Voltage

All-Solid-State Lithium-Ion Batteries. ACS Energy Lett. *9*, 38–47. https://doi.org/10.1021/acsenergylett.3c02307.

24. Song, Z., Wang, T., Yang, H., Kan, W.H., Chen, Y., Yu, Q., Wang, L., Zhang, Y., Dai, Y., Chen, H., et al. (2024). Promoting high-voltage stability through local lattice distortion of halide solid electrolytes. Nat. Commun. *15*, 1481. https://doi.org/10.1038/s41467-024-45864-1.
25. Wang, Q., Zhou, Y., Wang, X., Guo, H., Gong, S., Yao, Z., Wu, F., Wang, J., Ganapathy, S., Bai, X., et al. (2024). Designing lithium halide solid electrolytes. Nat. Commun. *15*, 1050. https://doi.org/10.1038/s41467-024-45258-3.
26. Ye, Y., Geng, J., Zuo, D., Niu, K., Chen, D., Lin, J., Chen, X., Woo, H.J., Zhu, Y., and Wan, J. (2024). High-Voltage Long-Cycling All-Solid-State Lithium Batteries with High-Valent-Element-Doped Halide Electrolytes. ACS Nano *18*, 18368–18378. https://doi.org/10.1021/acsnano.4c02678.
27. Zhang, S., Xu, Y., Wu, H., Pang, T., Zhang, N., Zhao, C., Yue, J., Fu, J., Xia, S., Zhu, X., et al. (2024). A Universal Self-Propagating Synthesis of Aluminum-Based Oxyhalide Solid-State Electrolytes. Angew. Chem. Int. Ed. Engl. *63*, e202401373. https://doi.org/10.1002/anie.202401373.
28. Zhang, G., Shi, X., Su, Q., Sun, Y., Lu, Y., Liu, K., Li, Z., Liu, H., and Zhang, L. (2024). Halide-sulfide bilayer electrolytes for LiFePO 4 -based all-solid-state batteries. Green Chem. *26*, 7971–7979. https://doi.org/10.1039/D4GC01640H.
29. Zhou, L., Kwok, C.Y., Shyamsunder, A., Zhang, Q., Wu, X., and Nazar, L.F. (2020). A new halospinel superionic conductor for high-voltage all solid state lithium batteries. Energy Environ. Sci. *13*, 2056–2063. https://doi.org/10.1039/D0EE01017K.
30. Zhou, L., Zuo, T.-T., Kwok, C.Y., Kim, S.Y., Assoud, A., Zhang, Q., Janek, J., and Nazar, L.F. (2022). High areal capacity, long cycle life 4 V ceramic all-solid-state Li-ion batteries enabled by chloride solid electrolytes. Nat. Energy *7*, 83–93. https://doi.org/10.1038/s41560-021-00952-0.
31. Kwak, H., Han, D., Lyoo, J., Park, J., Jung, S.H., Han, Y., Kwon, G., Kim, H., Hong, S.-T., Nam, K.-W., et al. (2021). New Cost-Effective Halide Solid Electrolytes for All-Solid-State Batteries: Mechanochemically Prepared Fe 3+ -Substituted Li 2 ZrCl 6. Adv. Energy Mater. *11*, 2003190. https://doi.org/10.1002/aenm.202003190.
32. Rosenbach, C., Walther, F., Ruhl, J., Hartmann, M., Hendriks, T.A., Ohno, S., Janek, J., and Zeier, W.G. (2023). Visualizing the Chemical Incompatibility of Halide and Sulfide-Based Electrolytes in Solid-State Batteries. Adv. Energy Mater. *13*, 2203673. https://doi.org/10.1002/aenm.202203673.
33. Schlautmann, E., Weiß, A., Maus, O., Ketter, L., Rana, M., Puls, S., Nickel, V., Gabbey, C., Hartnig, C., Bielefeld, A., et al. (2023). Impact of the Solid Electrolyte Particle Size Distribution in Sulfide-Based Solid-State Battery Composites. Adv. Energy Mater. *13*, 2302309. https://doi.org/10.1002/aenm.202302309.
34. Koerver, R., Aygün, I., Leichtweiß, T., Dietrich, C., Zhang, W., Binder, J.O., Hartmann, P., Zeier, W.G., and Janek, J. (2017). Capacity Fade in Solid-State Batteries: Interphase Formation and Chemomechanical Processes in Nickel-Rich Layered Oxide Cathodes and Lithium Thiophosphate Solid Electrolytes. Chem. Mater. *29*, 5574–5582. https://doi.org/10.1021/acs.chemmater.7b00931.
35. Aktekin, B., Sedykh, A.E., Müller-Buschbaum, K., Henss, A., and Janek, J. (2024). The Formation of Residual Lithium Compounds on Ni-Rich NCM Oxides: Their Impact on the Electrochemical Performance of Sulfide-Based ASSBs. Adv. Funct. Mater. *34*, 2313252. https://doi.org/10.1002/adfm.202313252.
36. Kaeli, E., Jiang, Z., Yang, X., Choy, E.P.K.L., Liang, N.B., Barks, E., Wang, S., Kang, S.D., and Chueh, W.C. (2025). Decoupling first-cycle capacity loss mechanisms in sulfide solid-state batteries. Energy Environ. Sci. *18*, 1452–1463. https://doi.org/10.1039/D4EE04908J.
37. Minnmann, P., Strauss, F., Bielefeld, A., Ruess, R., Adelhelm, P., Burkhardt, S., Dreyer, S.L., Trevisanello, E., Ehrenberg, H., Brezesinski, T., et al. (2022). Designing Cathodes and Cathode Active Materials for Solid-State Batteries. Adv. Energy Mater. *12*, 2201425. https://doi.org/10.1002/aenm.202201425.
38. Shi, B.-X., Yusim, Y., Sen, S., Demuth, T., Ruess, R., Volz, K., Henss, A., and Richter, F.H. (2023). Mitigating Contact Loss in Li 6 PS 5 Cl-Based Solid-State Batteries Using a Thin Cationic Polymer Coating on NCM. Adv. Energy Mater. *13*, 2300310.
39. Shi, B.-X., Weber, F., Yusim, Y., Demuth, T., Vettori, K., Münchinger, A., Titvinidze, G., Volz, K., Henss, A., Berger, R., et al. (2025). Lithiated polymer coating for interface stabilization in Li 6 PS 5 Cl-based solid-state batteries with high-nickel NCM. J. Mater. Chem. A *13*, 2600–2614. https://doi.org/10.1039/D4TA07265K.
40. Conforto, G., Ruess, R., Schröder, D., Trevisanello, E., Fantin, R., Richter, F.H., and Janek, J. (2021). Quantification of the Impact of Chemo-Mechanical Degradation on the Performance and Cycling Stability of NCM-Based Cathodes in Solid-State Li-Ion Batteries. J. Electrochem. Soc. *168*, 070546. https://doi.org/10.1149/1945-7111/ac13d2.
41. Zhang, W., Weber, D.A., Weigand, H., Arlt, T., Manke, I., Schröder, D., Koerver, R., Leichtweiss, T., Hartmann, P., Zeier, W.G., et al. (2017). Interfacial Processes and Influence of Composite Cathode Microstructure Controlling the Performance of All-Solid-State Lithium Batteries. ACS Appl. Mater. Interfaces *9*, 17835–17845. https://doi.org/10.1021/acsami.7b01137.
42. Ruhl, J., Riegger, L.M., Ghidiu, M., and Zeier, W.G. (2021). Impact of Solvent Treatment of the Superionic Argyrodite Li 6 PS 5 Cl on Solid-State Battery Performance. Adv. Energy Sustain. Res. *2*, 2000077. https://doi.org/10.1002/aesr.202000077.
43. Kissel, M., Schosland, M., Töws, J., Kalita, D., Schneider, Y., Kessler-Kühn, J., Schröder, S., Schubert, J., Frankenberg, F., Kwade, A., et al. (2025). Quantifying the Impact of Cathode Composite Mixing Quality on Active Mass Utilization and Reproducibility of Solid-State Battery Cells. Adv. Energy Mater. *15*, 2405405. https://doi.org/10.1002/aenm.202405405.
44. Merola, L., Singh, V.K., Palmer, M., Eckhardt, J.K., Benz, S.L., Fuchs, T., Nazar, L.F., Sakamoto, J., Richter, F.H., and Janek, J. (2024). Evaluation of Oxide|Sulfide Heteroionic Interface Stability for Developing Solid-State Batteries with a Lithium-Metal Electrode: The Case of LLZO|-Li6PS5Cl and LLZO|Li7P3S11. ACS Appl. Mater. Interfaces *16*, 54847–54863. https://doi.org/10.1021/acsami.4c11597.
45. Liu, Z., Tao, J., Jiang, H., Wu, Y., Lin, L., Yang, Y., Chen, Y., Huang, Z., and Lin, Y. (2025). Deciphering Interfacial Stability of Sulfide and Halide-Based Electrolytes via Operando X-ray Photoelectron Spectroscopy. Nano Lett. *25*, 4605–4612. https://doi.org/10.1021/acs.nanolett.5c00564.
46. Zhang, H., Yu, P., Cui, Z., Jin, H., Tang, W., Zhao, C., Lei, J., Liang, S., Shi, Z., Wang, J., et al. (2025). Enhancing Compatibility of Halide with Sulfide-Electrolytes via High Oxygen Incorporation for Robust Solid-State Batteries. Adv. Funct. Mater. *35*, e10497. https://doi.org/10.1002/adfm.202510497.
47. Zuo, T.-T., Rueß, R., Pan, R., Walther, F., Rohnke, M., Hori, S., Kanno, R., Schröder, D., and Janek, J. (2021). A mechanistic investigation of the Li10GeP2S12|LiNi1-x-yCoxMnyO2 interface stability in all-solid-state lithium batteries. Nat. Commun. *12*, 6669. https://doi.org/10.1038/s41467-021-26895-4.
48. Kim, W., Noh, J., Lee, S., Yoon, K., Han, S., Yu, S., Ko, K.-H., and Kang, K. (2023). Aging Property of Halide Solid Electrolyte at the Cathode Interface. Adv. Mater. *35*, e2301631. https://doi.org/10.1002/adma.202301631.
49. Panchal, A.A., Pennebaker, T.N.T., Sebti, E., Li, Y., Li, Y., Clément, R.J., and Canepa, P. (2024). Compatibility of Halide Bilayer Separators for All-Solid-State Batteries. ACS Energy Lett. *9*, 5935–5944. https://doi.org/10.1021/acsenergylett.4c02590.
50. Pennebaker, T., Sebti, E., Panchal, A., Huang, C.-J., Trenikhina, Y., Li, T., Li, Y., Li, Y., Kelly, S., Meng, Y.S., et al. (2025). Establishing the Compatibility of Anolytes and Catholytes in Dual Electrolyte Solid-State Batteries. Preprint at ChemRxiv. https://doi.org/10.26434/chemrxiv-2025-chtzv.

51. Fuchs, T., Ortmann, T., Becker, J., Haslam, C.G., Ziegler, M., Singh, V.K., Rohnke, M., Mogwitz, B., Peppler, K., Nazar, L.F., et al. (2024). Imaging the microstructure of lithium and sodium metal in anode-free solid-state batteries using electron backscatter diffraction. Nat. Mater. *23*, 1678–1685. https://doi.org/10.1038/s41563-024-02006-8.

52. Walther, F., Randau, S., Schneider, Y., Sann, J., Rohnke, M., Richter, F.H., Zeier, W.G., and Janek, J. (2020). Influence of Carbon Additives on the Decomposition Pathways in Cathodes of Lithium Thiophosphate-Based All-Solid-State Batteries. Chem. Mater. *32*, 6123–6136. https://doi.org/10.1021/acs.chemmater.0c01825.

53. Koerver, R., Walther, F., Aygün, I., Sann, J., Dietrich, C., Zeier, W.G., and Janek, J. (2017). Redox-active cathode interphases in solid-state batteries. J. Mater. Chem. A *5*, 22750–22760. https://doi.org/10.1039/C7TA07641J.

54. Henderson, J.D., Pearson, L., Nie, H.-Y., and Biesinger, M.C. (2025). X-Ray Photoelectron Spectroscopy Analysis of Indium and Indium-Containing Compounds. Surf. Interface Anal. *57*, 81–97. https://doi.org/10.1002/sia.7356.

55. McGuire, G.E., Schweitzer, G.K., and Carlson, T.A. (1973). Core electron binding energies in some Group IIIA, VB, and VIB compounds. Inorg. Chem. *12*, 2450–2453. https://doi.org/10.1021/ic50128a045.

56. Wei, W., Wei, Z., Li, R., Li, Z., Shi, R., Ouyang, S., Qi, Y., Philips, D.L., and Yuan, H. (2022). Subsurface oxygen defects electronically interacting with active sites on In2O3 for enhanced photothermocatalytic CO2 reduction. Nat. Commun. *13*, 3199. https://doi.org/10.1038/s41467-022-30958-5.

57. Wang, K., Ren, Q., Gu, Z., Duan, C., Wang, J., Zhu, F., Fu, Y., Hao, J., Zhu, J., He, L., et al. (2021). A cost-effective and humidity-tolerant chloride solid electrolyte for lithium batteries. Nat. Commun. *12*, 4410. https://doi.org/10.1038/s41467-021-24697-2.

58. Wang, X.-R., Zeng, Y.-X., Zhang, J., Huang, W., Ma, H.-P., and Zhang, Q.-C. (2024). Electronic properties of ZrO 2 films fabricated via atomic layer deposition on 4H-SiC and Si substrates. Mater. Res. Express *11*, 015902. https://doi.org/10.1088/2053-1591/ad1e0a.

59. Sarma, D.D., and Rao, C.N.R. (1980). XPES studies of oxides of second- and third-row transition metals including rare earths. J. Electron Spectrosc. Relat. Phenom. *20*, 25–45. https://doi.org/10.1016/0368-2048(80)85003-1.

60. Colón, J.L., Thakur, D.S., Yang, C.-Y., Clearfield, A., and Martini, C.R. (1990). X-ray photoelectron spectroscopy and catalytic activity of α-zirconium phosphate and zirconium phosphate sulfophenylphosphonate. J. Catal. *124*, 148–159. https://doi.org/10.1016/0021-9517(90)90111-V.

61. Jeon, H.-J., Subramanian, Y., and Ryu, K.-S. (2024). Variation of electrochemical performance of Li2ZrCl6 halide solid electrolyte with Mn substitution for all-solid-state batteries. J. Power Sources *602*, 234343. https://doi.org/10.1016/j.jpowsour.2024.234343.

62. Jellinek, F., Pollak, R.A., and Shafer, M.W. (1974). X-ray photoelectron spectra and electronic structure of zirconium trisulfide and triselenide. Mater. Res. Bull. *9*, 845–856. https://doi.org/10.1016/0025-5408(74)90121-4.

63. Xu, T., Ma, D., Li, T., Yue, L., Luo, Y., Lu, S., Shi, X., Asiri, A.M., Yang, C., and Sun, X. (2020). Enhanced electrocatalytic N2-to-NH3 fixation by ZrS2 nanofibers with a sulfur vacancy. Chem. Commun. *56*, 14031–14034. https://doi.org/10.1039/D0CC05917J.

64. Jeon, S., Park, K.-H., Cho, W., Jeong, G., Yu, J., Park, Y.J., and Kim, K. (2025). Hydrochloric acid-free synthesis of LiNbOCl4 superionic conductor for all-solid-state Li batteries. Solid State Ionics *421*, 116791. https://doi.org/10.1016/j.ssi.2025.116791.

65. Fontaine, R., Caillat, R., Feve, L., and Guittet, M.J. (1977). Déplacement chimique ESCA dans la série des oxydes du niobium. J. Electron Spectrosc. Relat. Phenom. *10*, 349–357. https://doi.org/10.1016/0368-2048(77)85032-9.

66. Ma, Q., and Rosenberg, R.A. (2003). Angle-resolved X-ray photoelectron spectroscopy study of the oxides on Nb surfaces for superconducting r.f. cavity applications. Appl. Surf. Sci. *206*, 209–217. https://doi.org/10.1016/S0169-4332(02)01238-2.

67. Chia, X., Ambrosi, A., Lazar, P., Sofer, Z., and Pumera, M. (2016). Electrocatalysis of layered Group 5 metallic transition metal dichalcogenides (MX 2 , M = V, Nb, and Ta; X = S, Se, and Te). J. Mater. Chem. A *4*, 14241–14253. https://doi.org/10.1039/C6TA05110C.

68. Özer, N., Rubin, M.D., and Lampert, C.M. (1996). Optical and electrochemical characteristics of niobium oxide films prepared by sol-gel process and magnetron sputtering A comparison. Sol. Energy Mater. Sol. Cells *40*, 285–296. https://doi.org/10.1016/0927-0248(95)00147-6.

69. Nefedov, V.I., Firsov, M.N., and Shaplygin, I.S. (1982). Electronic structures of MRhO2, MRh2O4, RhMO4 and Rh2MO6 on the basis of X-ray spectroscopy and ESCA data. J. Electron Spectrosc. Relat. Phenom. *26*, 65–78. https://doi.org/10.1016/0368-2048(82)87006-0.

70. Jain, A., Ong, S.P., Hautier, G., Chen, W., Richards, W.D., Dacek, S., Cholia, S., Gunter, D., Skinner, D., Ceder, G., et al. (2013). Commentary: The Materials Project: A materials genome approach to accelerating materials innovation. APL Mater. *1*. https://doi.org/10.1063/1.4812323.

71. Aktekin, B., Kataev, E., Riegger, L.M., Garcia-Diez, R., Chalkley, Z., Becker, J., Wilks, R.G., Henss, A., Bär, M., and Janek, J. (2024). Operando Photoelectron Spectroscopy Analysis of Li 6 PS 5 Cl Electrochemical Decomposition Reactions in Solid-State Batteries. ACS Energy Lett. *9*, 3492–3500. https://doi.org/10.1021/acsenergylett.4c01072.

72. Wu, X., Villevieille, C., Novák, P., and El Kazzi, M. (2018). Monitoring the chemical and electronic properties of electrolyte-electrode interfaces in all-solid-state batteries using operando X-ray photoelectron spectroscopy. Phys. Chem. Chem. Phys. *20*, 11123–11129. https://doi.org/10.1039/C8CP01213J.

73. Pavan, M., Münch, K., Benz, S.L., Bernges, T., Henss, A., Zeier, W.G., and Janek, J. (2025). Role and Evolution of FeS 2 Cathode Microstructure in Argyrodite-Based All-Solid-State Lithium–Sulfur Batteries. Chem. Mater. *37*, 3185–3196. https://doi.org/10.1021/acs.chemmater.4c03315.

74. Lee, D., Cui, Z., Goodenough, J.B., and Manthiram, A. (2024). Interphase Stabilization of LiNi0.5 Mn1.5 O4 Cathode for 5 V-Class All-Solid-State Batteries. Small *20*, e2306053.

75. Wang, S., Bai, Q., Nolan, A.M., Liu, Y., Gong, S., Sun, Q., and Mo, Y. (2019). Lithium Chlorides and Bromides as Promising Solid-State Chemistries for Fast Ion Conductors with Good Electrochemical Stability. Angew. Chem. *131*, 8123–8127.

76. Wilhelm, R., Schuster, R., Kutsch, T., Qian, S., Mahl, J., Kratky, T., Wandt, J., Crumlin, E.J., and Gasteiger, H.A. (2025). Exploring the Electrochemical Stability Window of an All-Solid-State Composite Cathode via a Novel Operando Tender XPS Setup. ACS Appl. Mater. Interfaces *17*, 38571–38586. https://doi.org/10.1021/acsami.5c01672.

77. Dewald, G.F., Ohno, S., Kraft, M.A., Koerver, R., Till, P., Vargas-Barbosa, N.M., Janek, J., and Zeier, W.G. (2019). Experimental Assessment of the Practical Oxidative Stability of Lithium Thiophosphate Solid Electrolytes. Chem. Mater. *31*, 8328–8337. https://doi.org/10.1021/acs.chemmater.9b01550.

78. Schwietert, T.K., Arszelewska, V.A., Wang, C., Yu, C., Vasileiadis, A., de Klerk, N.J.J., Hageman, J., Hupfer, T., Kerkamm, I., Xu, Y., et al. (2020). Clarifying the relationship between redox activity and electrochemical stability in solid electrolytes. Nat. Mater. *19*, 428–435. https://doi.org/10.1038/s41563-019-0576-0.

79. Wang, S., Xu, X., Cui, C., Zeng, C., Liang, J., Fu, J., Zhang, R., Zhai, T., and Li, H. (2022). Air Sensitivity and Degradation Evolution of Halide Solid State Electrolytes upon Exposure. Adv. Funct. Mater. *32*. https://doi.org/10.1002/adfm.202108805.

80. Strauss, F., Teo, J.H., Schiele, A., Bartsch, T., Hatsukade, T., Hartmann, P., Janek, J., and Brezesinski, T. (2020). Gas Evolution in Lithium-Ion Batteries: Solid versus Liquid Electrolyte. ACS Appl. Mater. Interfaces *12*, 20462–20468. https://doi.org/10.1021/acsami.0c02872.

81. Newnham, J.A., Kondek, J., Hartel, J., Rosenbach, C., Li, C., Faka, V., Gronych, L., Glikman, D., Schreiner, F., Wind, D.D., et al. (2025). Correlation between the Coherence Length and Ionic Conductivity in LiNbOCl 4 via the Anion Stoichiometry. Chem. Mater. *37*, 4130–4144. https://doi.org/10.1021/acs.chemmater.5c00627.

82. You, I., Singh, B., Cui, M., Goward, G., Qian, L., Arthur, Z., King, G., and Nazar, L.F. (2025). A facile route to plastic inorganic electrolytes for all-solid state batteries based on molecular design. Energy Environ. Sci. *18*, 478–491. https://doi.org/10.1039/D4EE03944K.

83. Randau, S., Weber, D.A., Kötz, O., Koerver, R., Braun, P., Weber, A., Ivers-Tiffée, E., Adermann, T., Kulisch, J., Zeier, W.G., et al. (2020). Benchmarking the performance of all-solid-state lithium batteries. Nat. Energy *5*, 259–270. https://doi.org/10.1038/s41560-020-0565-1.

84. Palmer, M., Qian, L., Singh, V.K., Merola, L., Carlson, E., Haslam, C., Janek, J., Nazar, L.F., and Sakamoto, J. (2025). Contact mechanics and electrochemical properties of the Li6.5La3Zr1.5Ta0.5O12|Li2.25Zr0.75Fe0.25Cl6 hetero-electrolyte interface in a low-pressure regime. Solid State Ionics *428*, 116948. https://doi.org/10.1016/j.ssi.2025.116948.

85. Yanagihara, S., Huebner, J., Huang, Z., Inoishi, A., Akamatsu, H., Hayashi, K., and Ohno, S. (2025). Compatibility of Halide Electrolytes in Solid-State Li–S Battery Cathodes. Chem. Mater. *37*, 109–118. https://doi.org/10.1021/acs.chemmater.4c02159.

86. Koç, T., Hallot, M., Quemin, E., Hennequart, B., Dugas, R., Abakumov, A.M., Lethien, C., and Tarascon, J.-M. (2022). Toward Optimization of the Chemical/Electrochemical Compatibility of Halide Solid Electrolytes in All-Solid-State Batteries. ACS Energy Lett. *7*, 2979–2987. https://doi.org/10.1021/acsenergylett.2c01668.

87. Jin, F., Fadillah, L., Nguyen, H.Q., Sandvik, T.M., Liu, Y., García-Martín, A., Salagre, E., Michel, E.G., Stoian, D., Marshall, K., et al. (2024). Elucidating the Impact of Li3InCl6-Coated LiNi0.8Co0.15Al0.05O2 on the Electro-Chemo-Mechanics of Li6PS5Cl-Based Solid-State Batteries. Chem. Mater. *36*, 6017–6026. https://doi.org/10.1021/acs.chemmater.4c00515.

88. Kwak, H., Kim, J.-S., Han, D., Kim, J.S., Park, J., Kwon, G., Bak, S.-M., Heo, U., Park, C., Lee, H.-W., et al. (2023). Boosting the interfacial superionic conduction of halide solid electrolytes for all-solid-state batteries. Nat. Commun. *14*, 2459. https://doi.org/10.1038/s41467-023-38037-z.